# A Second-Order Moment Method Applied to Gas–Solid Risers

**Juhui Chen**
School of Energy Science and Engineering, Harbin Institute of Technology, Harbin 150001, China

**Shuyan Wang**
School of Petroleum Engineering, Northeast Petroleum University, Daqing 163318, China

**Dan Sun and Huilin Lu**
School of Energy Science and Engineering, Harbin Institute of Technology, Harbin 150001, China

**Dimitri Gidaspow**
Dept. of Chemical and Biological Engineering, Illinois Institute of Technology, Chicago, IL 60616

**Hongbin Yu**
School of Energy Science and Engineering, Harbin Institute of Technology, Harbin 150001, China

*DOI 10.1002/aic.13754*
*Published online March 12, 2012 in Wiley Online Library (wileyonlinelibrary.com).*

*Second-order moment method of particles is proposed on the basis of the kinetic theory of granular flow. Closure equations for the third-order velocity moments are presented to account for the increase of the probability of collisions of particles on the basis of the elementary kinetic theory and order of magnitude analysis. The boundary conditions for the set of equations describing flow of particles are proposed with the consideration of the momentum exchange by collisions between the wall and the particles. The distributions of velocity, concentration and moments of particles are predicted. Simulated results are compared with experimental data measured by Tartan and Gidaspow and Bhusarapu et al. in risers, and Tsuji et al. in a vertical pipe. The effects of the closure equations for the third-order velocity moments and the fluid-particle velocity correlation tensor on flow behavior of particles are analyzed.* © 2012 American Institute of Chemical Engineers *AIChE J,* 58: 3653–3675, 2012

*Keywords: second-order moments, computational fluid dynamics, kinetic theory of granular flow, Reynolds stresses, fluidization*

## Introduction

The Eulerian–Eulerian (two-fluid) model with kinetic theory of granular flow (KTGF) is widely used in the numerical simulations of circulating fluidized beds. This model is particularly appropriate when the particle loading is relatively high and can be applied with reasonable computation effort.[1] In the KTGF, the kinetic and collisional momentum transfer due to the collisions of particles is modeled following the Chapman-Enskog approach for dense gases.[2] This theory gives closures for the rheologic properties of the fluidized particles as a function of the local particle concentration and the fluctuating motion of the particles owing to particle–particle collisions. Associated with the random motion of the particles, a pseudo-temperature is defined as $\theta = (1/3)\sum C_i C_i$, where $C_i$ is the fluctuation velocity of particles in the direction $i$. The granular temperature arises from momentum transport being dominated by collisions between particles. Modeling of the collisional and kinetic transport mechanisms for the momentum and fluctuating kinetic energy of the particles yields a description of the momentum transport properties of particles as a function of granular temperature. Simulations using the KTGF have been reported by many researchers.[3–19] Detailed discussion on the development of granular flow models is provided by Gidaspow.[1] The most significant application of KTGF to fluidization is reviewed by Arastoopour[20] and Gidaspow[21] in the Flour-Daniel AIChE lecture.

The granular temperature is defined as a measure of the mean kinetic fluctuation energy of particles. It comprises an important characterization of the velocity fluctuations of particles. Gidaspow et al.[22] measured granular temperature of 75 $\mu$m FCC particles in a circulating fluidized bed by means of a charge-coupled device (CCD). From measured velocity distribution of particles, the granular temperature was calculated from the axial and the lateral variances of the particles. They found that the axial variance is larger than the lateral variance. The granular temperature increases, reaches maxima, and then decreases with the increase of concentration of particles. Jung et al.[23] measured particle motion in a bubbling fluidized bed using a CCD camera technique. They found that the granular temperature in the axial direction is larger than that in the lateral direction. Two types of fluctuations in the velocity are identified in the gas-fluidized bed.

Correspondence concerning this article should be addressed to H. Yu at huilin@hit.edu.cn.

The first is known as the particle granular temperature that corresponds to the instantaneous variance in the velocity distribution. The second is the time-averaged variance of the mean velocity and is termed the Reynolds stresses. Xie et al.[24] used a diffusing wave spectroscopy (DWS) to measure the displacement of glass beads in a fluidized bed, and demonstrated that the spatial variations in the granular temperature are significant in a fluidized bed. Holland et al.[25] measured particle motion in the bubbling fluidized bed by a magnetic resonance technique (MR). Experiments showed that the granular temperature in the axial direction exceeds the granular temperature in the horizontal directions by a factor of 3 to 5. These suggest the granular temperature used in KTGF does not fully reveal the transport and loss of energy due to collisions and flow behavior of particles in fluidized beds.

Grad[26] developed the method of moments to the Boltzmann equation, and solved the Boltzmann equation for simple (elastic) gases using a third order approximation of the particle velocity distribution. In theory, with a third-order truncation, the 20 unknown variables are determined by 20 distinct transport equations: the continuity, momentum, granular temperature equations and the second- and third-moment equations. Grad[26] proposed to simplify this system of 20 unknown variables to 13 unknown variables by making a contraction on the third-order tensor. Jenkins et al.[27] used Grad's 13-moment method to obtain the single-particle velocity distribution function which allows solving the integral forms for the collisional rate of change of any particle property. Jenkins and Richman[28] developed a linear theory (perturbation analysis) which gives analytical solutions for mean flux of momentum and energy, the mean dissipation rate, and an expression for the particle velocity probability density function. Richman[29] introduced an anisotropic Maxwell distribution function, dependent on all second-order moments of the fluctuating velocities, and used all the second-order moment balances to solve the dilute, steady, homogeneous shear flows. Strumendo and Canu[30] derived a method of moment that account for the anisotropy based on a generalization of the Chapman-Enskog expansion, and apply the method of moments to predict the behavior of fast flow of smooth, identical spheres in a chute and circulating fluidized bed.[31] Simonin[32] adopted a moment method based on the Grad[26] approach to simulate particle-laden jets in dilute gas-particle flows.[33] Recently, the quadrature-based third-order moment method is proposed by Fox[34] on the basis of the KTGF containing terms for spatial transport, gravity, fluid drag, and particle–particle collisions in the dilute gas-particle flows. Desjardin et al.[35] used a quadrature-based moment method to show the limitations of the two-fluid model in predicting particle trajectory crossing, which leads to inconsistent predictions by the hydrodynamic model for all the velocity moments for nonzero Stokes numbers and to the overprediction of particle segregation. They indicate that the quadrature-based third-order moment method is valid to predict the anisotropy of particles flow. The model is extended to simulate of gas–solid two-phase flow from dilute to moderately dilute fluid-particle flows.[18,36] A second-order moment method is proposed by Dan et al.[37] based on the KTGF. The transport equations for the velocity moments are presented for the particle phase. Flow behavior of gas and particles is simulated by means of gas–solid two-fluid model with the second-order moment model of particles in the bubbling fluidized bed. They find that the simulated second-order moment and normal Reynolds stresses in the vertical direction is on average 1.5–2.3 and 4.5–6.0 times larger than that in the lateral direction in a bubbling fluidized bed.[38]

Experiments in fluidization mentioned earlier indicate the combination of the dissipation by collisions and the interaction between gas phase and solid phase causes the second-order velocity moments to be anisotropic. An anisotropic second-order velocity moments indicates that the motion of the particles is directly responsible for the transmission of momentum and transports their momentum and fluctuation kinetic energy around the system. This anisotropy demands the development of the method of moments. This motivates our interest in developing the kinetic theory model further. This work, therefore, aims to provide the second-order moment model used in the simulation of flow behavior in risers. Two different closure models for the third-order moments are proposed on the basis of an order of magnitude analysis proposed by Jenkins and Richman[28] and the elementary kinetic theory proposed by Grad,[27] respectively. The boundary conditions for solid phase are presented with the consideration of the energy dissipation by collisions between the wall and the particles. For the interfacial momentum force between gas and particle phases, a stitching function is used to smooth from the dilute regime to the dense regime. Simulated velocity and moments of particles are compared with experimental data measured by Tartan and Gidaspow[39] and Bhusarapu et al.[40] in the circulating fluidized beds and Tsuji et al.[41] in a vertical pipe.

## Gas–Solid Two-Phase Flow Model with a Second-Order Moment (SOM) for Solids

Computational fluid dynamics (CFD) attempts to rigorously solve the conservation laws of mass and momentum from first principles to yield results at high spatial and temporal resolution. In view of the large number of particles in the solid ensemble, the Eulerian–Eulerian two-fluid approach has been used. In this approach, both phases are considered to be continuous and fully interpenetrating and both phases are allowed to exist at the same point and at the same time. Such an idea is made possible by the introduction of a new dependent variable, the volume fraction, $\varepsilon_i$, of each phase $i$. The ensemble average of the two-fluid conservation equations leads to the appearance of certain extra terms in the averaged equations, and these must be closed. More details of the mathematical and theoretical basis of this approach can be found elsewhere.[1,42] In the following subsections, governing equations, determination of source and flux terms of the collisional rate of change, closure equation for the third-order moment, gas-particle velocity correlation tensor and boundary conditions are described.

### *Governing equations for gas phase*

The behavior of the gas phase is described by the classical continuity and momentum equations solved in multifluid models.[1] Assumed that there is no source of mass due to phase change or chemical reaction, the mass balance equation of gas phase is expressed by Eq. (T1-1) without reaction.

The momentum balance for the gas phase is given by the Navier-Stokes equation, modified to include an interphase momentum transfer term.[1] The equation of momentum for the mean motion is expressed by Eq. (T1-3). The viscous stress tensor is given in Eq. (T1-7). For simplifications, the constant viscosity of gas phase is used in the present simulations.

### *Transport equations for solid phase*

For simplicity, the following assumptions are made. Particles are smooth spheres of uniform diameter. The particles are noncohesive. The collisions between particles are supposed to be binary, instantaneous and inelastic. The probability of finding a sphere at a position $\mathbf{x}$ with a velocity $\mathbf{c}$ in the volume element $d\mathbf{x}$ and in the element of volume in the velocity space $d\mathbf{c}$ is $f(\mathbf{x},\mathbf{c},t)d\mathbf{x}d\mathbf{c}$, where $f(\mathbf{x},\mathbf{c},t)$ is the particle velocity probability density function. The fluctuation velocity is introduced, $\mathbf{C} = u - c$, where u is the mean velocity of particles. Considering a population of identical, smooth, rigid spheres, the transport equation for the mean particle property $<\phi>$ is[1,2]

$$\frac{D}{Dt}(n<\phi>)+\frac{\partial}{\partial \mathbf{x}}\cdot(n<\mathbf{C}\phi>)+<n\phi>\frac{\partial}{\partial \mathbf{x}}\cdot\mathbf{u}+n\frac{D\mathbf{u}}{Dt}\cdot <\frac{\partial\phi}{\partial \mathbf{C}}>-n<\mathbf{F}\cdot\frac{\partial\phi}{\partial \mathbf{C}}>+n<\mathbf{C}\frac{\partial\phi}{\partial \mathbf{C}}>:\frac{\partial \mathbf{u}}{\partial \mathbf{x}}=\mathrm{Coll}(\phi) \quad (1)$$

where $\mathbf{F}$ is the external force per unit of mass acting on a sphere. $n$ is the number density of particles. The collisional rate of change of particle property $\phi$ per unit volume, Coll($\phi$), is the integral, over all possible binary collisions, of the change of $\phi$ due to a binary collision multiplied by the probability of such a collision. The expression of Coll($\phi$) is[1,2]

$$\mathrm{Coll}(\phi)=\chi(\phi)-\nabla\cdot\psi(\phi) \quad (2)$$

$$\chi(\phi)=\frac{1}{2}\iiint_{\mathbf{g}\cdot\mathbf{k}>0}[(\phi_1'-\phi_1)+(\phi_2'-\phi_2)] f^{(2)}(\mathbf{x},\mathbf{c}_1,\mathbf{x}+\sigma\mathbf{k},\mathbf{c}_2,t)\sigma^2(\mathbf{g}\cdot\mathbf{k})d\mathbf{k}d\mathbf{c}_1d\mathbf{c}_2 \quad (3)$$

$$\psi(\phi)=-\frac{\sigma}{2}\iiint_{\mathbf{g}\cdot\mathbf{k}>0}(\phi_1'-\phi_1)f^{(2)}(\mathbf{x}-\frac{1}{2}\sigma,\mathbf{c}_1,\mathbf{x}+\frac{1}{2}\sigma\mathbf{k},\mathbf{c}_2,t)\times\sigma^2(\mathbf{g}\cdot\mathbf{k})d\mathbf{k}d\mathbf{c}_1d\mathbf{c}_2 \quad (4)$$

where $\sigma$ is the diameter of a particle. The first term on the right-hand side, $\chi(\phi)$, is the collisional source (or sink) term, which represents the loss of $\phi$ due to inelastic collisions. The flux term, $\psi(\phi)$ represents the transfer of $\phi$ during collision.

The moment $M_N$ is equal to the generic $(N+1)$th-order moment of the fluctuating velocities divided by the number density of particles $n$; besides the generic $(N+1)$th-order moment of the fluctuating velocities

$$M_N(\mathbf{x},t)=\overline{\underbrace{\mathbf{CC}\cdots\cdots\mathbf{C}}_{N}}=\frac{1}{n(x,t)}\int\underbrace{\mathbf{CC}\cdots\cdots\mathbf{C}}_{N}f(\mathbf{c},\mathbf{x},t)d\mathbf{c} \quad (5)$$

The transport equations for the moment of order $N$, can be obtained from Eq. 1 combining with Eqs. 3 and 4. Table 1 lists the model equations used in present simulations. The continuity equation of particles (zeroth-order moment $N = 0$, $M_0$) is shown in Eq. (T1-2).

The momentum equation of particles (first-order moment $N = 1$, $M_1$) is expressed

$$\frac{\partial}{\partial t}(\varepsilon_s\rho_s u_{si})+\frac{\partial}{\partial x_j}(\varepsilon_s\rho_s u_{si}u_{sj})=-\varepsilon_s\nabla p_g-\frac{\partial}{\partial x_j}\Pi_{2ij}+\beta(u_{gi}-u_{si})+\varepsilon_s\rho_s g_i \quad (6)$$

where $\Pi_{2ij}=[\varepsilon_s\rho_s M_{ij}+\psi_j(mC_i)]$ is the effective stress tensor. The second term on the right-hand side (RHS) represents the transport of momentum by velocity fluctuations and by collisions, whereas the remaining terms on the RHS represent the influence of the forces acting on the particles.

The transport equation for the second-order moment of velocity fluctuation is obtained from Eq. 1 using $\phi = C_iC_j$ and neglecting the pressure fluctuations as done for the momentum equation. The equation for the second-order moment of particles ($N = 2$, $M_2$) is expressed

$$\frac{\partial}{\partial t}(\varepsilon_s\rho_s M_{ij})+\frac{\partial}{\partial x_k}(\varepsilon_s\rho_s u_{sk}M_{ij})=-\frac{\partial}{\partial x_k}\Xi_{kij}-\Pi_{2ik}\frac{\partial u_{sj}}{\partial x_k}-\Pi_{2jk}\frac{\partial u_{si}}{\partial x_k}+\beta(C_{gi}C_{sj}-M_{ij})+\chi(mC_iC_j) \quad (7)$$

where $\Xi_{kij}=[\varepsilon_s\rho_s M_{kij}+\psi_k(mC_iC_j)]$. The first term on the RHS represents the transport of stress by velocity fluctuations and collisions. The second and third terms represent the production of stress by the mean velocity gradient. The fourth term represents the interaction with the continuous phase (a production or a destruction term). The last term represents the interactions due to collisions.

### *Determination of source term and flux term of the collisional rate of change*

In Eqs. 3 and 4, the pair distribution function $f^{(2)}$ is the probability of finding a pair of particles 1 and 2 centered at $\mathbf{x}_1$,$\mathbf{x}_2$ with a velocity $\mathbf{c}_1$,$\mathbf{c}_2$ in the volume element $d\mathbf{x}_1$,$d\mathbf{x}_2$ and the velocity range $d\mathbf{c}_1$,$d\mathbf{c}_2$, respectively. A particle 1 ($\mathbf{x}_1$,$\mathbf{c}_1$) collides with a particle 2 ($\mathbf{x}_2$,$\mathbf{c}_2$) if the center of particle 1 is located in an elementary cylinder of volume $\sigma^2(\mathbf{g}\cdot\mathbf{k})d\mathbf{k}dt$ (at this point of the derivation), where the relative velocity is $\mathbf{g} = \mathbf{c}_1 - \mathbf{c}_2$, and the unit vector $\mathbf{k}$ is defined by $d\mathbf{k} = \mathbf{x} - \mathbf{x}_1$ with $\mathbf{g}\cdot\mathbf{k} \geq 0$ (this condition means that collision is possible). According to Chapman and Cowling,[2] the pair distribution function $f^{(2)}(\boldsymbol{x}_1, \boldsymbol{c}_1, \boldsymbol{x}_2, \boldsymbol{c}_2, t)$ can be expressed as the product of the two particle velocity probability density functions $f_1(\boldsymbol{x}_1, \boldsymbol{c}_1, t)$ and $f_2(\boldsymbol{x}_2, \boldsymbol{c}_2, t)$

$$f^{(2)}(\mathbf{x}_1,\mathbf{c}_1,\mathbf{x}_2,\mathbf{c}_2,t)=g_0(\mathbf{x})f_1(\mathbf{x},\mathbf{c}_1,t)f_2(\mathbf{x}+\sigma\mathbf{k},\mathbf{c}_2,t) \quad (8)$$

where the radial distribution function at contact, $g_0(x) \geq 1.0$, represents the increase of the binary collision probability when the suspension becomes denser. Grad wrote the particle velocity probability density function as a series of Hermite polynomials.[26] The particle velocity probability density function can then be written as a third-order approximation which is a reasonable assumption if the flow is not varying too quickly (this assumption is not valid, for instance, in strong shock waves).

$$f_1=f_0\left(H^0+a_i^{(1)}H_i^1+\frac{1}{2!}a_{ij}^{(2)}H_{ij}^2+\frac{1}{3!}a_{ijm}^{(3)}H_{ijm}^3\right) \quad (9)$$

where the distribution function $f_0(\mathbf{x},\mathbf{c},t)$ is expressed in terms of the particle number density $n$, the magnitude of the velocity fluctuation $C$ and the granular temperature $\theta$, by[26]

$$f_0(\boldsymbol{x},\boldsymbol{c},t)=\frac{n}{(2\pi\theta)^{3/2}}\exp\left(-\frac{\boldsymbol{C}^2}{2\theta}\right) \quad (10)$$

**Table 1. Equations of Gas–Solid Flow for Second-Order Moment Method in Circulating Fluidized Beds**

(1) Continuity equations of gas and particles

$$\frac{\partial}{\partial t}(\varepsilon_{\mathrm{g}}\rho_{\mathrm{g}}) + \frac{\partial}{\partial x_i}(\varepsilon_{\mathrm{g}}\rho_{\mathrm{g}}u_{\mathrm{g}i}) = 0 \tag{T1-1}$$

$$\frac{\partial}{\partial t}(\varepsilon_{\mathrm{s}}\rho_{\mathrm{s}}) + \frac{\partial}{\partial x_i}(\varepsilon_{\mathrm{s}}\rho_{\mathrm{s}}u_{\mathrm{s}i}) = 0 \tag{T1-2}$$

(2) Conservation of momentum of gas phase

$$\frac{\partial}{\partial t}(\varepsilon_{\mathrm{g}}\rho_{\mathrm{g}}u_{\mathrm{g}i}) + \frac{\partial}{\partial x_j}(\varepsilon_{\mathrm{g}}\rho_{\mathrm{g}}u_{\mathrm{g}i}u_{\mathrm{g}j}) = -\varepsilon_{\mathrm{g}}\frac{\partial p_{\mathrm{g}}}{\partial x_i} + \frac{\partial \tau_{\mathrm{g}ij}}{\partial x_j} - \beta(u_{\mathrm{g}i} - u_{\mathrm{s}i}) + \varepsilon_{\mathrm{g}}\rho_{\mathrm{g}}g_i \tag{T1-3}$$

(3) Conservation of momentum of solids (first-order moment)

$$\frac{\partial}{\partial t}(\varepsilon_{\mathrm{s}}\rho_{\mathrm{s}}u_{\mathrm{s}i}) + \frac{\partial}{\partial x_j}(\varepsilon_{\mathrm{s}}\rho_{\mathrm{s}}u_{\mathrm{s}i}u_{\mathrm{s}j}) = -\varepsilon_{\mathrm{s}}\frac{\partial p_g}{\partial x_i} - \frac{\partial}{\partial x_j}[\varepsilon_{\mathrm{s}}\rho_{\mathrm{s}}M_{ij} + \psi_j(mC_i)] + \beta(u_{\mathrm{g}i} - u_{\mathrm{s}i}) + \varepsilon_{\mathrm{s}}\rho_{\mathrm{s}}g_i \tag{T1-4}$$

(4) Equation for the second-order moment of particles

$$\begin{aligned}\frac{\partial}{\partial t}(\varepsilon_s\rho_sM_{ij}) + \frac{\partial}{\partial x_k}(\varepsilon_s\rho_su_{sk}M_{ij}) &= -\frac{\partial}{\partial x_k}[\varepsilon_s\rho_sM_{kij} + \psi_k(mC_iC_j)] \\ -[\varepsilon_s\rho_sM_{ik} + \psi_k(mC_i)]\frac{\partial u_{sj}}{\partial x_k} - [\varepsilon_s\rho_sM_{jk} + \psi_k(mC_j)]\frac{\partial u_{si}}{\partial x_k} &+ \beta(C_{gi}C_{sj} - M_{ij}) + \chi(mC_iC_j)\end{aligned} \tag{T1-5}$$

(5) Closure equations of particles (model A)

$$M_{kij} = -\frac{[1 + \frac{6}{5}(1+e)\varepsilon_{\mathrm{s}}g_0]M_{kl}}{\frac{3}{5}\left[\frac{3\beta}{\varepsilon_{\mathrm{s}}\rho_{\mathrm{s}}} + \frac{2}{5\sigma}(1+e)(49-33e)\varepsilon_{\mathrm{s}}g_0\sqrt{\frac{\theta}{\pi}}\right]}\frac{\partial M_{ij}}{\partial x_l} \tag{T1-6}$$

(6) Constitutive relations

(a) Gas phase viscous stress tensor

$$\tau_{\mathrm{g}ij} = \varepsilon_{\mathrm{g}}\mu_{\mathrm{g}}\left[\frac{\partial u_{\mathrm{g}i}}{\partial x_j} + \frac{\partial u_{\mathrm{g}j}}{\partial x_i}\right] - \frac{2}{3}\varepsilon_{\mathrm{g}}\mu_{\mathrm{g}}\frac{\partial u_{\mathrm{g}k}}{\partial x_k}\delta_{ij} \tag{T1-7}$$

(b) Interphase momentum exchange

$$\beta = (1-\varphi)\left[150\frac{\varepsilon_{\mathrm{s}}^2\mu_{\mathrm{g}}}{\varepsilon_{\mathrm{g}}\sigma^2} + 1.75\frac{\rho_{\mathrm{g}}\varepsilon_{\mathrm{s}}|u_{\mathrm{g}} - u_{\mathrm{s}}|}{\sigma}\right] + \varphi\frac{3}{4}C_D\frac{\rho_{\mathrm{g}}\varepsilon_{\mathrm{s}}|u_{\mathrm{g}} - u_{\mathrm{s}}|}{\sigma}\varepsilon_{\mathrm{g}}^{-2.65} \tag{T1-8}$$

$$\varphi = \frac{\arctan[150 \times 1.75(\varepsilon_{\mathrm{g}} - 0.8)]}{\pi} + 0.5 \tag{T1-9}$$

$$C_{\mathrm{D}} = \begin{cases} \frac{24}{Re}(1 + 0.15Re^{0.687}) & Re<1000 \\ 0.44 & Re \geq 1000 \end{cases} \tag{T1-10a}$$

$$Re = \frac{\rho_{\mathrm{g}}\varepsilon_{\mathrm{g}}\sigma(u_{\mathrm{g}} - u_{\mathrm{s}})}{\mu_{\mathrm{g}}} \tag{T1-10b}$$

(c) Source of the collisional rate of change

$$\begin{aligned}\chi(mC_iC_j) = -\frac{8}{\sigma}\rho_{\mathrm{s}}\varepsilon_{\mathrm{s}}^2(1+e)(1-e)g_0\sqrt{\frac{\theta}{\pi}}\theta\delta_{ij} - \frac{6}{5}\rho_{\mathrm{s}}\varepsilon_{\mathrm{s}}^2(1+e)g_0\theta\left[\left(e-2\right)\left(\frac{\partial u_{si}}{\partial x_j} + \frac{\partial u_{sj}}{\partial x_i}\right) + \left(e - \frac{1}{3}\right)\frac{\partial u_{sk}}{\partial x_k}\delta_{ij}\right] \\ -\frac{24}{5\sigma}\rho_{\mathrm{s}}\varepsilon_{\mathrm{s}}^2(1+e)(3-e)g_0\sqrt{\frac{\theta}{\pi}}(M_{ij} - \theta\delta_{ij})\end{aligned} \tag{T1-11}$$

(*Continued*)

**Table 1. (Continued)**

(d) Flux of the collisional rate of change

$$\psi_i(mC_j) = 2\rho_s\varepsilon_s^2(1+e)g_0\theta\delta_{ij} - \frac{4}{5}\rho_s\varepsilon_s^2\sigma(1+e)g_0\sqrt{\frac{\theta}{\pi}}\left[\left(\frac{\partial u_{si}}{\partial x_j}+\frac{\partial u_{sj}}{\partial x_i}\right)+\frac{\partial u_{sk}}{\partial x_k}\delta_{ij}\right] + \frac{4}{5}\rho_s\varepsilon_s^2(1+e)g_o(M_{ij}-\theta\delta_{ij}) \tag{T1-12}$$

$$\psi_k(mC_iC_j) = -\frac{4}{5}\rho_s\varepsilon_s^2\sigma(1+e)g_0\sqrt{\frac{\theta}{\pi}}\left(\frac{\partial\theta}{\partial x_i}\delta_{jk}+\frac{\partial\theta}{\partial x_j}\delta_{ik}+\frac{\partial\theta}{\partial x_k}\delta_{ij}\right) + \frac{1}{5}\rho_s\varepsilon_s^2(1+e)g_0\left(4M_{ijk}+M_{ill}\delta_{jk}+M_{jll}\delta_{ik}\right) \tag{T1-13}$$

(e) Source due to hydrodynamic interactions

$$\beta\overline{C_{gi}C_{sj}} = \frac{162\varepsilon_s\mu_g^2}{\rho_s\sigma^3\sqrt{\theta}}\left[S_v\left|\mathbf{u}_g-\mathbf{u}_s\right|^2\delta_{ij}+(S_h-S_v)\left(u_{gi}-u_{si}\right)\left(u_{gj}-u_{sj}\right)\right] \tag{T1-14}$$

$$S_v = \frac{3R_o^2}{16\sqrt{\pi}g_0\left(1+3.5\sqrt{\varepsilon_s}+5.9\varepsilon_s\right)}\sqrt{\frac{\theta}{\theta_h}}\left[\frac{1}{2}\left(a_\theta^3-a_\theta^5\right)\mathbf{ln}\left(\frac{a_\theta+1}{a_\theta-1}\right)-\frac{2}{3}a_\theta^2+a_\theta^4\right] \tag{T1-15a}$$

$$S_h = \frac{3R_0^2}{16\sqrt{\pi}g_0\left(1+3.5\sqrt{\varepsilon_s}+5.9\varepsilon_s\right)}\sqrt{\frac{\theta}{\theta_h}}\left[\left(a_\theta^5+a_\theta\right)\mathbf{ln}\left(\frac{a_\theta+1}{a_\theta-1}\right)-\frac{2}{3}a_\theta^2-2a_\theta^4\right] \tag{T1-15b}$$

$$a_\theta^2 = \theta_h/(\theta_h-\theta_v) \tag{T1-15c}$$

$$R_0 = \frac{1+3(\varepsilon_s/2)^{0.5}+(135/64)\varepsilon_s\ln\varepsilon_s+17.14\varepsilon_s}{1+0.681\varepsilon_s-8.48\varepsilon_s^2+8.16\varepsilon_s^3} \tag{T1-15d}$$

(7) Boundary conditions

(a) Tangential velocity of particles

$$\varepsilon_s\rho_sM_{ik}+\psi_k(mC_i) = (1+e_{wt})\frac{\varepsilon_s\rho_s}{2}g_0M_{ik}+(1+e_{wt})\frac{\varepsilon_s\rho_s}{2}g_0\sqrt{\frac{\theta}{2\pi}}\left(1+\frac{M_{kk}}{\theta}\right)u_{si} \tag{T1-16}$$

(b) Second-order moment of particles for $mC_kC_k$

$$\varepsilon_s\rho_sM_{kkk}+\psi_k(mC_kC_k) = (1-e_{wn})(1+e_{wn})\varepsilon_s\rho_sg_0\theta\sqrt{\frac{\theta}{2\pi}}\left(3\frac{M_{kk}}{\theta}-1\right) \tag{T1-17}$$

(c) Second-order moment of particles for $mC_kC_i$

$$\varepsilon_s\rho_sM_{ikk}+\psi_k(mC_iC_k) = (1-e_{wn}e_{wt})\varepsilon_s\rho_sg_0\theta\sqrt{\frac{\theta}{2\pi}}\left(2\frac{M_{ik}}{\theta}\right)-e_{wn}(1+e_{wt})\frac{\varepsilon_s\rho_s}{2}g_0M_{kk}u_{si} \tag{T1-18}$$

(d) Second-order moment of particles for $mC_iC_j$

$$\varepsilon_s\rho_sM_{ijk}+\psi_k\left(mC_iC_j\right) = (1-e_{wt})(1+e_{wt})\varepsilon_s\rho_sg_0\theta\sqrt{\frac{\theta}{2\pi}}\left(\frac{M_{kk}}{2\theta}\delta_{ij}-\frac{1}{2}\delta_{ij}+\frac{M_{ij}}{\theta}\right) - e_{wt}(1+e_{wt})\frac{\varepsilon_s\rho_s}{2}g_0\left(M_{ik}u_{sj}+M_{jk}u_{si}\right)-(1+e_{wt})^2\frac{\varepsilon_s\rho_s}{2}g_0\sqrt{\frac{\theta}{2\pi}}\left(1+\frac{M_{kk}}{\theta}\right)u_{si}u_{sj} \tag{T1-19}$$

The Hermite polynomials are defined in terms of the derivatives of the distribution function $f_0$.

$$H^0 = 1, \quad H_i^1 = \frac{1}{f_0}\frac{\partial f_0}{\partial c_i} = -\frac{\boldsymbol{C}_i}{\theta} \tag{11a}$$

$$H_{ij}^2 = \frac{1}{f_0}\frac{\partial^2 f_0}{\partial\boldsymbol{c}_i\partial\boldsymbol{c}_j} = -\frac{\delta_{ij}}{\theta}+\frac{\boldsymbol{C}_i\boldsymbol{C}_j}{\theta^2} \tag{11b}$$

$$H_{ijm}^3 = \frac{1}{f_0}\frac{\partial^3 f_0}{\partial\boldsymbol{c}_i\partial\boldsymbol{c}_j\partial\boldsymbol{c}_m} = \frac{\boldsymbol{C}_i\delta_{jm}+\boldsymbol{C}_j\delta_{im}+\boldsymbol{C}_m\delta_{ij}}{\theta^2}-\frac{\boldsymbol{C}_i\boldsymbol{C}_j\boldsymbol{C}_m}{\theta^3} \tag{11c}$$

With Eq. 9, up to the third order velocity moments, the coefficients of the series expansion, $a_i^{(1)}$, $a_{ij}^{(2)}$, $a_{im,}^{(3)}$, can be related. Using Eqs. 8 and 11, the source term $\chi(\phi)$ and the flux term $\psi_i(\phi)$, can be written[26–28]

$$\chi(\phi) = \frac{1}{2}\iiint_{\mathbf{g}\cdot\mathbf{k}>0} \Delta_\chi(\phi) g_0 f_{01} f_{02} \sigma^2 (\mathbf{g}\cdot\mathbf{k}) d\mathbf{k} d\mathbf{c}_1 d\mathbf{c}_2 + \frac{\sigma}{4}\iiint_{\mathbf{g}\cdot\mathbf{k}>0} \Delta_\chi(\phi) g_0 f_{01} f_{02} \mathbf{k}\cdot\frac{\partial \ln(f_{02}/f_{01})}{\partial \mathbf{x}} \sigma^2 (\mathbf{g}\cdot\mathbf{k}) d\mathbf{k} d\mathbf{c}_1 d\mathbf{c}_2 + \frac{a_{ij}^{(2)}}{4}\iiint_{\mathbf{g}\cdot\mathbf{k}>0} \Delta_\chi(\phi) g_0 (f_{01} f_{02,ij} + f_{01,ij} f_{02}) \sigma^2 (\mathbf{g}\cdot\mathbf{k}) d\mathbf{k} d\mathbf{c}_1 d\mathbf{c}_2 + \frac{a_{ijk}^{(3)}}{12}\iiint_{\mathbf{g}\cdot\mathbf{k}>0} \Delta_\chi(\phi) g_0 (f_{01} f_{02,ijk} + f_{01,ijk} f_{02}) \sigma^2 (\mathbf{g}\cdot\mathbf{k}) d\mathbf{k} d\mathbf{c}_1 d\mathbf{c}_2 \tag{12}$$

$$\psi_i(\phi) = -\frac{\sigma}{2}\iiint_{\mathbf{g}\cdot\mathbf{k}>0} \Delta_\psi(\phi) g_0 f_{01} f_{02} \sigma^2 \mathbf{k}_i (\mathbf{g}\cdot\mathbf{k}) d\mathbf{k} d\mathbf{c}_1 d\mathbf{c}_2 - \frac{\sigma^2}{4}\iiint_{\mathbf{g}\cdot\mathbf{k}>0} \Delta_\psi(\phi) g_0 f_{01} f_{02} \mathbf{k}_i \mathbf{k}_j \frac{\partial \ln(f_{02}/f_{01})}{\partial \mathbf{x}} \sigma^2 (\mathbf{g}\cdot\mathbf{k}) d\mathbf{k} d\mathbf{c}_1 d\mathbf{c}_2 - \frac{\sigma a_{ij}^{(2)}}{4}\iiint_{\mathbf{g}\cdot\mathbf{k}>0} \Delta_\psi(\phi) g_0 (f_{01} f_{02,jk} + f_{01,jk} f_{02}) \sigma^2 \mathbf{k}_i (\mathbf{g}\cdot\mathbf{k}) d\mathbf{k} d\mathbf{c}_1 d\mathbf{c}_2 - \frac{\sigma a_{ijk}^{(3)}}{12}\iiint_{\mathbf{g}\cdot\mathbf{k}>0} \Delta_\psi(\phi) g_0 (f_{01} f_{02,ijk} + f_{01,ijk} f_{02} \sigma^2 \mathbf{k}_i (\mathbf{g}\cdot\mathbf{k}) d\mathbf{k} d\mathbf{c}_1 d\mathbf{c}_2 \tag{13}$$

where $\Delta_\chi(\phi) = (\phi_1' - \phi_1) + (\phi_2' - \phi_2)$ and $\Delta_\psi(\phi) = (\phi_1' - \phi_1)$. Both these integrations are performed analytically whereas the integration over $\mathbf{g}$ is performed numerically. Tables of integrals given by Chapman and Cowling[2] are useful for carrying out the analytical integration over $\mathbf{k}$. By definition for Eq. 11, the source term in the momentum equation is equal to zero

$$\chi(mC_i) = 0. \tag{14}$$

The source term in the second-order moment equation is expressed by Eq. (T1-11). It consists of three parts. The first part comes from the isotropic collisions of particles, where $e$ is the restitution coefficient of particles. The second part is induced by the spatial gradients of the mean fields of the solid phase, while the last term is the contribution of anisotropic fluctuating velocities, and is termed the "redistribution term" or "return-to-equilibrium term." By summing up the diagonal terms, $i = j$, and changing indices the source term for an isotropic flow is expressed

$$\chi(mC_iC_i) = -\frac{12}{\sigma}(1-e^2)\varepsilon_s^2 \rho_s g_0 \sqrt{\frac{\theta}{\pi}}\theta + 3(1-e^2)\varepsilon_s^2 \rho_s g_0 \theta \nabla\cdot\boldsymbol{u}_s \tag{15}$$

which is the same as the expression of the dissipation of fluctuating energy due to inelastic collision used in KTGF.[1]

The flux term $\psi_i(\phi)$represents the transfer of $\phi$ during collision of particles. The flux term in the momentum equation and the flux in the second-order moment equation are respectively expressed by Eqs. (T1-12) and (T1-13).

Note that the kinetic theory models and second-order moment method rely on the assumption that the particle phase Mach number is less than unity. This assumption arises due to the restrictions that are imposed when performing the Chapman-Enskog expansion, that is, used to derive kinetic theory based models of gas-particle flows. For monodisperse systems the Mach number of solid phase, $Ma$, is given as $Ma = u_s/\sqrt{\theta}$. From our simulations we find that the value of Mach number can be greater than unity in our domain simulations. However, we find that if we construct particle phase averages in the domain simulations, the particle phase Mach number is smaller than unity. For a flow of 530 $\mu$m glass beads in the riser, the averaged solid velocity and granular temperature shown in Figures 6 and 10 are 28 cm/s and 872 $(\mathrm{cm/s})^2$ at the height of 4.2 m (to be presented later). The averaged concentration of particles is 0.0097. The computed Mach number is 0.94. Therefore, the effect of Mach number in our simulations is small for the domain-averaged concentration of particles presented in this work. We suspect that as the domain-averaged concentration of particles decreases the violation of the finite Mach number condition will have a larger impact on the dynamics of the gas–solid flow.

### *The closure equation for the third-order moment*

The transport equations have been written up to the third-order moment. We use these equations with a third order approximation of the particle velocity probability density function to express a closed set of equations. The transport equation for the third-order moment ($N = 3$, $M_3$) is obtained from Eq. 1 using $\phi = C_iC_jC_m$ and neglecting the pressure fluctuations

$$\frac{\partial}{\partial t}(\varepsilon_s\rho_s M_{ijk}) + \frac{\partial}{\partial x_l}(\varepsilon_s\rho_s u_{sl} M_{ijk}) = -\frac{\partial}{\partial x_l}[\varepsilon_s\rho_s M_{lijk} + \psi_l(mC_iC_jC_k)] + M_{jk}\frac{\partial}{\partial x_l}\Pi_{2li} - \Xi_{ljk}\frac{\partial u_{si}}{\partial x_l} + M_{ik}\frac{\partial}{\partial x_l}\Pi_{2lj} - \Xi_{lik}\frac{\partial u_{sj}}{\partial x_l} + M_{ij}\frac{\partial}{\partial x_l}\Pi_{2lk} - \Xi_{lij}\frac{\partial u_{sk}}{\partial x_l} + \varepsilon_s\rho_s(\overline{F_iC_jC_k} - \overline{F_i}M_{jk}) + \varepsilon_s\rho_s(\overline{F_jC_iC_k} - \overline{F_j}M_{ik}) + \varepsilon_s\rho_s(\overline{F_kC_iC_j} - \overline{F_k}M_{ij}) + \chi(mC_iC_jC_k) \tag{16}$$

where the fourth-order moment is defined by $M_{lijk} = \langle C_lC_iC_jC_k\rangle$. The first term on the RHS represents the transport of the third-order moment by velocity fluctuations and collisions. The six following terms on the RHS represent the production by mean velocity gradients and by second-order moment gradients, respectively. The three remaining terms on the RHS represent the interactions with the gas phase and the interactions due to collisions, respectively. The last term is the source term by particle collisions. The moments $M_{ijk}$ are fully determined by a numerical solution of the set of nonlinear equations given by Eq. 16. However, the simplified forms of $M_{ijk}$ can be obtained using a term-by-term order of magnitude analysis.[27] To understand when this approximation is valid, let us define the following dimensionless quantities: $U_o$, $L_o$, and $\theta_o$, which are the characteristic values of velocity, length and granular temperature. The time derivatives in Eq. 16 can be neglected if $d_pU_o/L\sqrt{\theta_0}$ is small. Retaining the linear terms and neglecting the terms proportional to the mean transport and mean gradient effects, from Eq. 16 the closure equation for the third-order velocity moment is

$$M_{kij} = -\frac{M_{kl}}{\frac{3}{5}\left[\frac{3\beta}{\varepsilon_s\rho_s} + \frac{2}{5\sigma}(1+e)(49-33e)\varepsilon_s g_0\sqrt{\frac{\theta}{\pi}}\right]}\frac{\partial M_{ij}}{\partial x_l} \tag{17}$$

The first term in the denominator represents the influence of the interstitial gas. When there is no interstitial gas, Eq. 17 is identical to the results of Jenkins and Richman.[28]

For the isotropic flow that means the isotropy assumption (Boussinesq approximation) holds and without the consideration of the effect of the mean relative velocity between the gas phase and the solid phase, the closure equation for the third-order velocity moment proposed by Gidaspow[1] is expressed

$$M_{kii}^{G} = -\frac{25\sigma\sqrt{\pi\theta}}{32(1+e)\varepsilon_s g_0}\left[1+\frac{6}{5}(1+e)\varepsilon_s g_0\right]\frac{\partial\theta}{\partial x_k} \tag{18}$$

The ratio of $M_{kii}^{G}/M_{kii}$ from Eqs. 18 and 17 without interstitial gas is

$$\frac{M_{kii}^{G}}{M_{kii}} = \left[1+\frac{6}{5}(1+e)\varepsilon_s g_0\right] \tag{19}$$

Therefore, the modified closure equation for the third-order velocity moment is expressed

$$M_{kij} = -\frac{\left[1+\frac{6}{5}(1+e)\varepsilon_s g_0\right]M_{kl}}{\frac{3}{5}\left[\frac{3\beta}{\varepsilon_s\rho_s}+\frac{2}{5\sigma}(1+e)(49-33e)\varepsilon_s g_0\sqrt{\frac{\theta}{\pi}}\right]}\frac{\partial M_{ij}}{\partial x_l} \tag{20}$$

which is known as model A. This factor in the nominator represents the contribution of the increase of the binary collision probability since the correlation in particle velocity increases (influence of $g_0$). For the isotropic flow of particles and without interstitial gas, Eq. 20 is recovered to Eq. 18 used in KTGF.[1]

Note that present SOM model has been written up to the second-order moment. We use these equations with a third order moment approximation to express a closed set of equations. Recently, the third-order quadrature-based moment method is proposed by Fox.[34] and used to simulate flow behavior in the gas–solid system. The difference between the SOM model and the quadrature-based moment method is the closure of the third-order moments. In the quadrature-based moment method, the third-order moment transport equation is solved and uses a quadrature to compute its fluxes (i.e., the fourth-order moments). Whereas in the SOM model the third order moments are expressed from the lower order transported moments. Thus, these two methods are not of the same order.

### *Gas-particle velocity correlation tensor*

From studies on the dynamics of a single particle in a gas, two important mechanisms for the gas–solid interaction force are considered: drag force caused by velocity differences between gas and solid phases, and buoyancy caused by the gas pressure gradient. Other forces, such as virtual mass effect caused by relative acceleration between phases, Magnus force caused by particle spin and Basset history forces are not considered due to the large density difference between gas and solids. Thus, the external force per unit of mass acting on a sphere can be written as[1]

$$\mathbf{F} = -\frac{1}{\rho_s}\nabla p_g + \frac{\beta}{\varepsilon_s\rho_s}\left(u_{gi}-u_{si}\right)+\mathbf{g} \tag{21}$$

In this work, the Ergun equation[43] and the equation of Wen and Yu[44] are used for the calculation of the drag coefficient $\beta$. For solid concentrations greater than 0.2, the Ergun correlation[43] is used, whereas for values less than or equal to 0.2, the Wen and Yu expression[44] is used. This transition at the concentration of 0.2 makes the drag law discontinuous in solid concentration though it is continuous in Reynolds number. Physically, the drag force is a continuous function of both solid concentration and Reynolds number, and therefore the continuous forms of the drag law may be needed to correctly simulate gas–solid fluidized beds. To avoid discontinuity of the two correlations, a switch function $\varphi$ is proposed[45] to give a smooth transition from the dilute regime to the dense regime, and given in Eq. (T1-9). The drag coefficient is expressed by Eq. (T1-8).

Note that studies by Andrews et al.[9] and Heynderickx et al.[46] have introduced an effective drag coefficient closing the drag force. Both formulations predict a reduction of the drag coefficient by a factor 1.5–4, depending on the concentration of particles. Hence, it is possible that the effect of a drag coefficient approach on the flow behavior of gas and particles is further investigated.

The source of energy fluctuation is related to the autocorrelation of the force felt by particles

$$\overline{F_{d,i}C_j} = \frac{\beta}{\varepsilon_s\rho_s}\left(C_{gi}C_{sj}-M_{ij}\right) \tag{22}$$

These terms represent the mean rate of interfacial energy transfer (i.e., hydrodynamic interactions) as a result of the correlation between velocity fluctuations of gas phase and dispersed phases and extra dissipation owing to the fluctuating drag force acting on the particles in fluctuating motion. The first term corresponds to a source of the moment due to long-range gas-particle interactions, where disturbance in the gas turbulent flow field induced by the fluctuating motion of the neighboring particles enhances the particle fluctuating motion. The second term corresponds to a sink of the moments due to the fluctuating viscous drag force. There is no general agreement on how to model the gas–solid fluctuating velocity correlation. The velocity moments for dilute suspensions with isotropic Maxwellian distributions is proposed by Sangani et al.[47] The source due to hydrodynamic interactions $C_{gi}C_{sj}$ is expressed by Eq. (T1-14). Koch and Sangani[48] derived the vertical $S_v$ and horizontal $S_h$ components of the source tensor in the above expression for dilute sedimenting suspensions. We assume that the same expressions hold for dense suspensions. The vertical and horizontal components of the source tensor are given in Eq. (T1-15), where $\theta_h$ and $\theta_v$ are, respectively, the variance in the velocity components parallel and perpendicular to $(u_g-u_s)$. Note that Eq. (T1-14) is limited to suspensions with particles having large Stokes number ( $St \gg 1.0$ ).[48] The Stokes number is expressed by $St = 2m_S u_t/(3\pi\mu_g\sigma^2)$, where $m_s$ is the mass of particles, and $u_t$ is the terminal velocity of an isolated particle. If $St > \varepsilon_S^{-3/2}$, the collisional mechanism is dominant. If $\varepsilon_S^{-3/4} \le St \le \varepsilon_S^{-3/2}$, The viscous relaxation time is shorter than the collision time. If $1 \le St \le \varepsilon_S^{-3/4}$, the fluid-particle interactions are dominant. From our simulations given in Tables 2–4 we find that Stokes number is in the range of 300-15,000. Indeed, when solving the transport equations for the second-order velocity moment, the source tensor $C_{gi}C_{sj}$ appears in Eq. (T1-5). Equation (T1-14) is limited to small Reynolds numbers ($Re_t = u_t\sigma\rho_g/\mu_g$) and large Stokes numbers, but they are algebraic. Therefore, for suspensions where these conditions are fulfilled, one does not need to

solve a transport equation for the source tensor. Indeed, the form of the transport equation for the source tensor is a key point in the formulation of the models. It can be obtained using a method similar to the one adopted in the KTGF.[49] Thus, more research is needed in this field.

### *Boundary conditions*

Boundary conditions have to be specified at the wall for the mean velocities of gas and particle phases and the second-order moment of particles. For gas phase, the no-slip boundary condition is used. The mean velocity fields are given by $u_g = 0$.

The boundary conditions at the wall are determined to take a balance around a volume element that includes the wall and during an interval time. For a dilute flow, the boundary conditions of velocity and the second-order moments of solid phases were derived by Strumendo.[50] Details are found in Strumendo and Canu.[30] The balance of particle property $\phi$ (averaged respect to the fluctuations) inside the volume element $d$v and during time $d$t is

$$\begin{aligned}&(\text{inlet} - \text{outlet}) \text{ of } \phi \text{ across } d\text{v in } d\text{t}\\ &\quad +(\text{production} - \text{dissipation of } \phi \text{ across } d\text{v in } d\text{t})\\ &+(\text{production} - \text{dissipation of } \phi \text{ on the surface A in } d\text{t}) = 0\end{aligned} \tag{23}$$

For the property $\phi(\mathbf{c})$, the term at the left hand side of Eq. 23 represents a flux term, and the term at the right hand side of Eq. 23 is the amount of the property $\phi(\mathbf{c})$ dissipated against the walls. It can be expressed as[30]

$$\iiint f(\boldsymbol{C},\boldsymbol{r},t)\phi\boldsymbol{C}d\boldsymbol{C} = \iiint\limits_{\boldsymbol{c}\cdot\boldsymbol{k}>0} f(\boldsymbol{C},\boldsymbol{r},t)(\phi-\phi')\boldsymbol{C}d\boldsymbol{C} \tag{24}$$

The collision of a particle against the wall is described by means of the wall restitution coefficient $e_{wn}$ and the tangential wall restitution coefficient $e_{wt}$. For the normal and tangential directions, the following expressions hold

$$\boldsymbol{C}'_n = -e_{wn}\boldsymbol{C}_n \tag{25a}$$

$$\boldsymbol{C}_t - \boldsymbol{C}'_t = (1+e_{wt})\boldsymbol{C}_t \tag{25b}$$

Assuming a Grad[27] expansion truncated to the second order moments, From Eq. 9, the particle velocity probability distribution function is

$$f = g_0 f_0 (1 + a_{ij}^{(2)} H_{ij}^{(2)}) \tag{26}$$

Here, the radial distribution function $g_0$ is introduced to modify the effect of collisions of particles at the walls. From Eqs. 24 to 26, the boundary equation of the tangential velocity of particles is expressed by Eq. (T1-16). The normal velocity of particles is set at zero. The energy flux at the wall is related to the normal shear stress, wall-particle collisional properties (normal and tangential restitution coefficient). The boundary condition from the second-order moment balance along vertical direction $k$ is expressed by Eqs. (T1-17)–(T1-19).

For initial conditions, the simulations start with a specified homogeneous field in a solid concentration. The gas velocity is initialized from the minimum fluidizing velocity. The pressure field is initialized from a reference pressure and the particle velocity is set to small quantities. At the inlet, all velocities of gas and particles are specified. At the outlet, the pressure is set to be 1 atm.

The simulations are carried out with the CFD code second-order moments-flow with interphase exchanges (SOM-FIX) which is based on the CFD K-FIX code. The original K-FIX is initially developed for gas–liquid flows, and later on adapted to deal with gas–solid flows.[1] K-FIX is based on a numerical method developed by Harlow and Amsden[51] which is an extension of the implicit continuous-fluid Eulerian technique developed by Harlow and Amsden.[52] The K-FIX code is previously used to model the flow in fluidized beds with the original KTGF.[1,12] The SOM-FIX code is incorporated with the second-order moment method to replace the granular temperature equation. In this study, a two-dimensional (2-D) computational fluid dynamics (CFD) model is used with the SOM model in the riser. The maximum residual at convergence for continuity, momentum and second-order moment equations are $1 \times 10^{-3}$, $1 \times 10^{-4}$, and $1 \times 10^{-4}$ with the time step of $1 \times 10^{-5}$ s. The simulations are run for 50 s for each case. The time-averaged results are obtained by averaging results from 15.0 to 50 s. Numerical results with the model presented in previous section are evaluated by following three experiments.

## Computed Results and Analysis

### *Numerical considerations and grid refinement study*

Moments profiles can be obtained from simulations by means of Lagrangian simulation, Grad's method and quadrature-based method.[53,54] Lostec et al.[55] compared the results using the quadrature methods and the Grad's method in a particle laden flow. Here, we will consider flow behavior of particles predicted using the SOM model and KTGF, and compare to quadrature-based method simulation results by Passalacqua et al.[18] in a periodic vertical channel. However, we should emphasize that this is not our target application and hence we do not demonstrate the ability of the SOM model to capture gas-particle flows. The diameter and length of the channel is 0.1m and 1.0 m, respectively. The diameter and density of particles are 80 $\mu$m and 1500 kg/m$^3$. The average gas velocity is 2.0 m/s. The particle phase is initialized with zero velocity and a uniform concentration of particles in all computational cells is 0.04. The gas density and viscosity are 1.2 kg/m$^3$ and $1.74 \times 10^{-4}$ (Pa s).[18]

Figure 1 shows the distribution of concentration of particles predicted by the SOM and KTGF models. The simulations predicted by Passalacqua et al.[18] using the quadrature-based method are also given in. Roughly, all simulations show the concentration of particles is high in the center of the channel. The difference is obvious for three different models. The concentration of particles predicted by Passalacqua et al.[18] using the quadrature-based method decreases from the walls, reaches a minimum, and then increases. However, both the SOM model and KTGF give the concentration of particles increases from the wall to the center of the channel. The simulated axial velocity of particles is also shown in Figure 1. All simulations can produce the similar profiles of axial velocity of particles. Predicted axial velocity of particles is high at the center, and decreases near the walls. Near the walls, the axial velocity of particles simulated by means of the SOM model is larger than that is

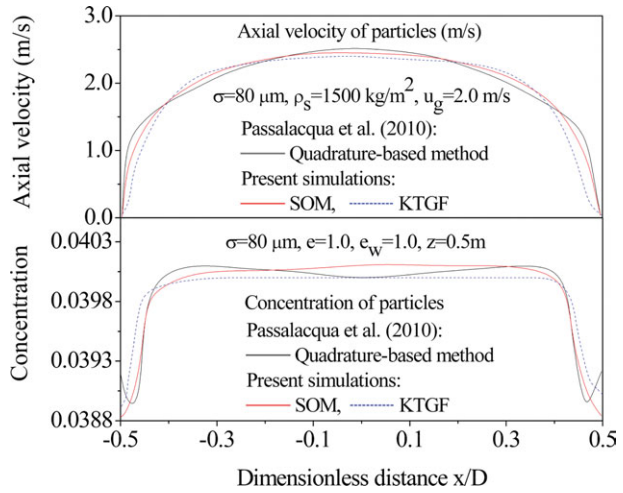


**Figure 1. Distribution of concentration and axial velocity of particles.**

**[Color figure can be viewed in the online issue, which is available at wileyonlinelibrary.com.]**

obtained with KTGF, but is lower than those obtained with the quadrature-based method predicted by Passalacqua et al.[18]

Figure 2 shows the distribution of normal second-order moments predicted by the SOM model. The values of normal second-order moment $M_{zz}$ are larger than that of $M_{xx}$. Roughly, both $M_{zz}$ and $M_{xx}$ are low in the center of the channel and large near the walls. From simulated second-order moments, the granular temperature is computed, and shown in Figure 2. The granular temperature predicted by Passalacqua et al.[18] by means of the quadrature-based method is also given in Figure 2. Simulations show the granular temperature is high near the walls, and low in the center of the channel. The granular temperature predicted by means of the SOM model is larger than that using KTGF. The granular temperature predicted by Passalacqua et al.[18] using the quadrature-based method show a granular temperature peak very close to the wall. This means an increase in the fluctuating velocity of particles near the wall. The granular temperature profile predicted by the SOM model and KTGF does not show temperature peaks next to the walls. This might explain the differences in the shape of the solid concentration profile observed in Figure 1.

Note that the simulated results using the SOM model and KTGF show a difference from those predicted by Passalacqua et al.[18] by means of the quadrature-based method. However it is necessary to keep in mind the difference of the order of these methods, moments of $M_0$, $M_1$, and $M_2$ being transported in the SOM model and the granular temperature $\theta$ used in KTGF. While the moments of $M_0$, $M_1$, $M_2$, and $M_3$ are considered in the quadrature-based method.[18] Hence, further comparisons using the SOM model, KTGF and quadrature-based method are required in gas–solid flow systems.

Figure 3 shows the measured and simulated axial velocity and granular temperature at three different gird sizes in a riser.[39] The diameter and height of the riser is 76.2 mm and 6.9 m. In 2-D simulations, the uniform grids of different sizes ($14 \times 121$ for coarse grids, $20 \times 168$ for mid grids, and $28 \times 212$ for finer grids) are tested. It is found that the finer and the mid grids give the same resolution and are in agreement with experimental data.[39] The times required to compute one second of real simulation time by means of the SOM model and KTGF are also given in Figure 3. One case requires up to 8–9 days for 50.0 s of real simulation time, while it needs 5–6 days by means of the KTGF on a PC (80 GB hard disk, 1 Gb RAM, and 2.4GHz CPU). This can be attributed to the equation structures contained in the SOM model. The conservation equations are discretized in finite differences equations.[51,52,56] The continuity equations are discretized implicitly, while the momentum equations and the second-order moment equations are discretized over a staggered mesh. In the momentum and the second-order moment equations the convective terms are treated explicitly and all other terms are treated implicitly. The scalar variables are set at the center of the cells while the vector variables are placed at the boundaries of the cells. The calculations are started with a guessed pressure field, that is, either the specified initial condition or the pressure field computed in the previous time step. Using this guessed pressure field, the velocities are calculated from the momentum equations and the second-order moments are calculated from the second-order moment equations. The continuity equation of solid phase is solved using the updated velocities to compute the concentration of particles. $\varepsilon_g$ is then computed. Using $\varepsilon_g$ and updated velocities is computed the gas phase mass residue from continuity equation for gas phase. This residue is used as a convergence criterion. For convergence, the gas pressure is corrected in each cell at a time until convergence is attained. The computations proceed until the entire computational domain is covered. Hence, the additional equations for second-order moments greatly increase the complexity of numerical simulations. Note that when one considers 3-D simulations, the difference of computing times between the SOM model and KTGF is expected to be even larger.

### *Tartan and Gidaspow experiment in a circulating fluidized bed*

Tartan and Gidaspow[39] measured particle velocity and concentration by means of a CCD camera and $\gamma$-ray densitometer for flow of 530 $\mu$m glass beads (Geldart B) in a circulating fluidized bed. The riser made of acrylic tube of 7.62 cm ID with a height of 699 cm. Instantaneous particle-

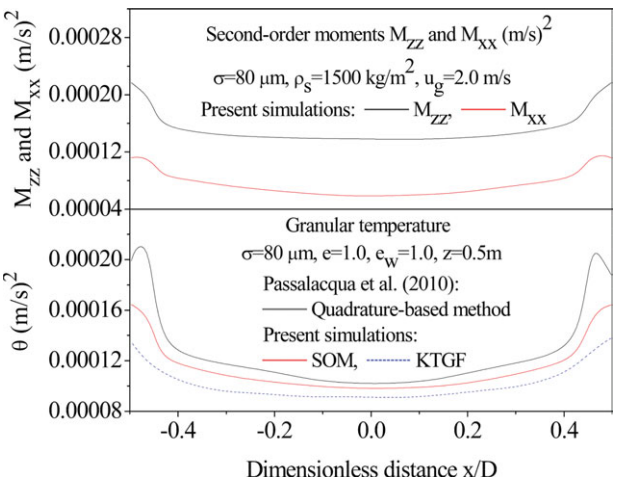


**Figure 2. Profile of normal second-order moments and granular temperature.**

**[Color figure can be viewed in the online issue, which is available at wileyonlinelibrary.com.]**

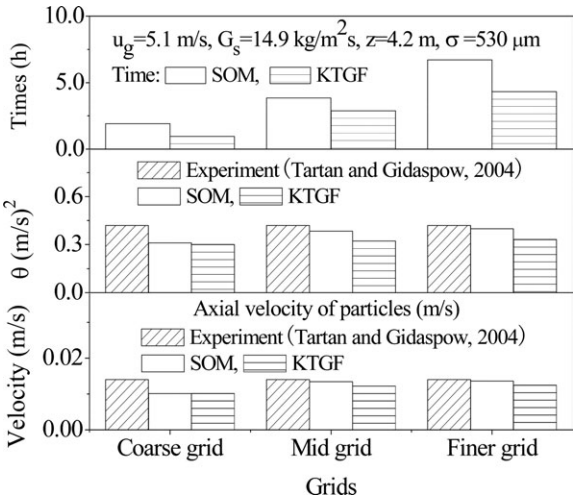


**Figure 3. Measured and simulated velocity and granular temperature and computing times.**

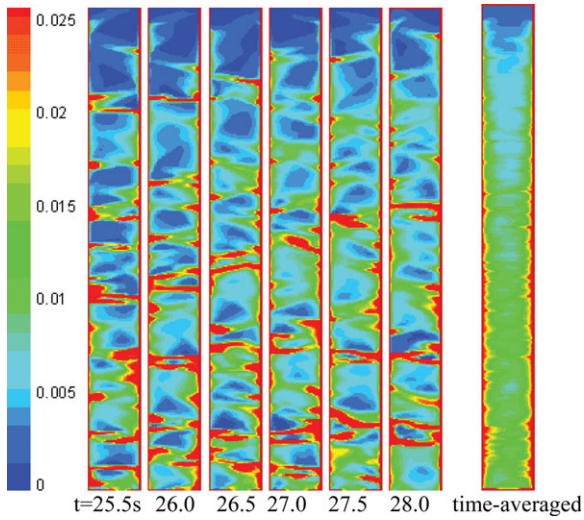


**Figure 4. Instantaneous concentration of particles in a riser.**

**[Color figure can be viewed in the online issue, which is available at wileyonlinelibrary.com.]**

velocity distributions are computed from measured trajectory of particle, and the standard deviation is calculated from velocity histogram of particles. Therefore, the second-order moments and granular temperature of particles are determined. Detail descriptions of the experiments can be found in Tartan and Gidaspow.[39] In this study, the restitution coefficient of particles–particles and particles-wall are 0.95 and 0.6 which were used by Tartan and Gidaspow[39] in the simulations of riser. The tangential restitution coefficient of particles-wall is 0.3 that was used by Goldschmidt et al.[57] in the numerical simulations of bubbling fluidized beds. The parameters used in the present computations are given in Table 2.

Figure 4 shows the instantaneous concentration of particles from the beginning of the simulation. Particles flow from inlet at the bottom, and pass through by gas. After 2.5 s, particles reach the middle section of the riser and as particles continue to move upward, the density of particles in the riser increases until a statistically quasi-steady-state condition is reached. The nonhomogeneities of concentration field are evident. The behavior of the flow is characterized by a formation of particle clusters at the walls. Such dense portions of solid undergo a zigzag motion, thus favoring a particle circulation in the riser. It should be noted how a move left at the right wall are mostly associated with a move right at the left wall, but more complex combinations are possible, too. A characteristic feature of the flow is the oscillating motion of solid clusters from one wall to the other through the center line of the riser. The time-averaged concentration of particles is computed. Results show that a core-annular flow structure, which has a high solid concentration near the walls and low in the center regime, is formed in the riser.

**Table 2. Simulation Conditions and System Properties**

| | Tartan and Gidaspow[39] | Present Simulations |
|---|---|---|
| Riser diameter | 7.62 cm | 7.62 cm |
| Riser inlet diameter | 4.23 cm | 4.23 cm |
| Riser height | 699 cm | 699 cm |
| Particle size | 530 $\mu$m | 530 $\mu$m |
| Particle density | 2460 kg/m$^3$ | 2460 kg/m$^3$ |
| Restitution coefficient of particles | 0.98, 0.95, 0.89 | 0.95 |
| Normal restitution coefficient of wall-particles | 0.60 | 0.60 |
| Tangential restitution coefficient of wall-particles | / | 0.3 |
| Solid mass flux | 1.42 g/cm$^2$ s | 1.42 g/cm$^2$ s |
| Gas superficial velocity | 490 cm/s | 490 cm/s |
| Gas density | 1.2 kg/m$^3$ | 1.2 kg/m$^3$ |
| Stokes number $St$ | 159,407 | 159,407 |
| Reynolds number $Re_t$ | 1917 | 1917 |
| Time step | $5 \times 10^{-5}$ s | $1 \times 10^{-5}$ s |

Figure 5 shows the radial distribution of time-averaged concentration of particles at the superficial gas velocity and solid mass flux of 4.9 m/s and 14.2 kg/m$^2$s. Both simulations by KTGF and experimental data of time-averaged concentration from Tartan and Gidaspow[39] are also given in. Simulations and experiments show that the high concentration of particles is near the wall and low in the center. Present model agrees with experiments. At the center regime, the predictions using the SOM model are lower than that from simulations by means of KTGF. However, it is reverse near the wall. The difference between the simulations using the SOM model and KTGF is obvious.

The radial distribution of axial velocity of particles is shown in Figure 6 at the superficial gas velocity and solid mass flux of 4.9 m/s and 14.2 kg/m$^2$s. Both simulations and experiments show the high velocity of particles is in the center, and low near the wall. We find that simulations predicted by Tartan and Gidaspow[39] are close to their measurements. While present simulations give higher than that measurements in the center regime. However, the trends are the same. Given the time averaged profiles of solid concentration in Figure 5 combined with the axial particle velocity in Figure 6, it is evident that the flow along the riser has a core-annular structure with the high velocity and low concentration in the center regime, and the low velocity and high concentration of particles near the wall. The solid mainly accumulates and moves upward in the riser. The main flow characteristics of the riser are predicted by present modeling results.

Figure 7 shows the instantaneous concentration of particles and normal second-order moment $M_{zz}$ as a function of

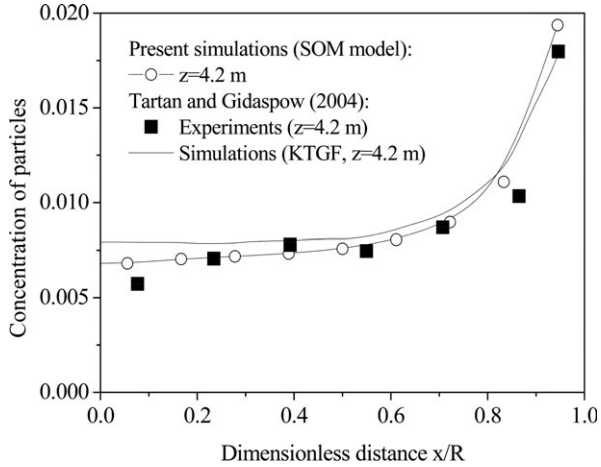


**Figure 5. Simulated and measured concentration of particles.**

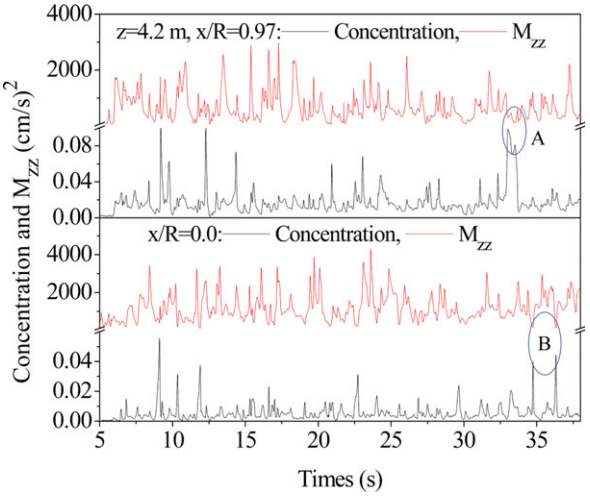


**Figure 7. Instantaneous concentration and normal second-order moment $M_{zz}$ of particles.**

**[Color figure can be viewed in the online issue, which is available at wileyonlinelibrary.com.]**

times at two positions at the superficial gas velocity and solid mass flux of 4.9 m/s and 14.2 kg/m$^2$s. The local concentration of particles is oscillations. A high instantaneous concentration of particles means the motion of cluster. Thus, the simulated instantaneous solid concentrations convey the message that the clustering phenomenon is significant near the wall region and can also occur in the core of the riser. The standard deviation of solid concentration is calculated from simulated instantaneous concentration of particles. The values of the standard deviation are 0.0049 and 0.0137 at the $x/R = 0.0$ and 0.97, respectively. This indicates that more oscillations are found near the walls due to the formation and breakage of clusters. As it can be seen, the normal second-order moment $M_{zz}$ is larger at $x/R = 0$ than that at $x/R = 0.97$. We also find the instantaneous normal second-order moment $M_{zz}$ is high when the local instantaneous concentration of particles is low, seeing points A and B. This indicates the motion of clusters has a low normal second-order moment, while the dispersed particles have a high instantaneous second-order moment $M_{zz}$. This means that during the cluster formation the second-order moments of particles are reduced. In the phase of the decrease of local concentration of particles, the cluster may vanish in the form of dispersed particles. The particles are accelerated and simultaneously the gas phase is decelerated due to the two-way coupling between the gas and the solid phases, thus an increase in their relative velocity. This results in the increase of second-order moments of dispersed particles. Using laser Doppler velocimetry for 800 $\mu$m cork particles, Breault et al.[58] found that the granular temperature of a particle cluster is different from the dispersed particles granular temperature. The measured mean granular temperature of clusters is 0.032 m$^2$/s$^2$. For dispersed particles, the granular temperatures range from about 0.4 to 0.9 m$^2$/s$^2$. From simulations, we find the SOM model yields predictions of fluctuation of particles observed in experiments.[58]

From the simulated instantaneous second-order moments, the time-averaged values are calculated. Figure 8 shows the time-averaged normal second-order moments $M_{zz}$ and $M_{xx}$ of particles as a function of the radial positions at the superficial gas velocity and solid mass flux of 4.9 m/s and 14.2 kg/m$^2$s. The instantaneous particle velocity was measured by means of the CCD color video camera.[39] In this technique, the particle velocity was measured by means of a length of a

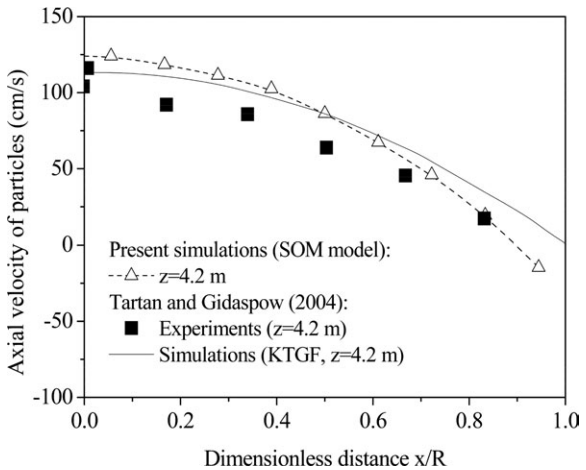


**Figure 6. Simulated and measured axial velocity of particles.**

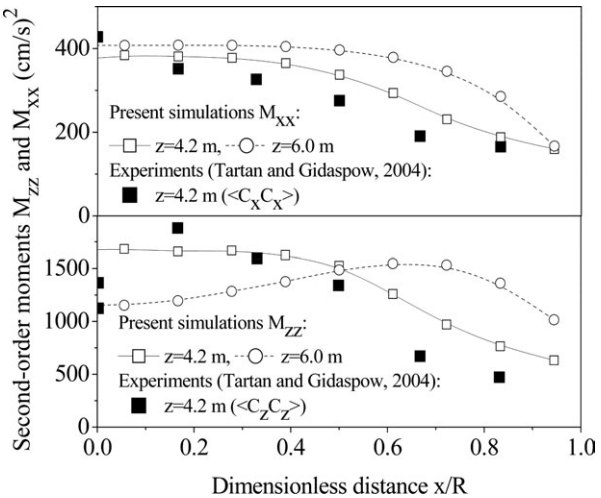


**Figure 8. Distribution of axial and radial normal second-order moments.**

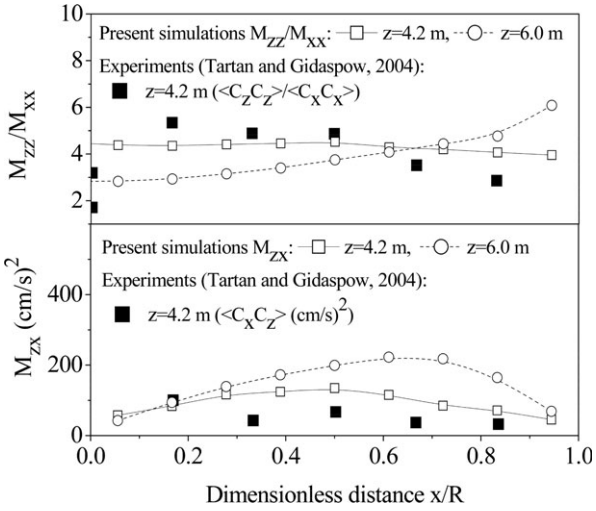


**Figure 9. Distribution of second-order cross moment and ratio of $M_{zz}/M_{xx}$.**

streak divided by the elapsed time. From measured instantaneous particle velocity, the normal stresses per unit bulk density are computed. Both simulations and experiments show that the normal second-order moments are high in the center regime and low near the wall. The variances of fluctuating velocity in the direction of flow $M_{zz}$ are 2 to 6 times higher than those in the radial direction. This is due to the high gradient of axial velocity. This indicates the isotropy does not hold. The time-averaged second-order cross moment $M_{zx}$ are plotted in Figure 9 as a function of radial positions. The $M_{zx}$ values are low at the center and monotonically increase toward to the wall. Near the wall there is gradually a decrease as shown Figure 9. Present simulations overestimate the values of the second-order cross moment. The ratio of $M_{zz}$ and $M_{xx}$ is plotted in Figure 9. The value of the ratio is in the range of 2-6. The anisotropy of the normal second moments is obvious.

Figure 10 shows the distribution of granular temperature at the superficial gas velocity and solid mass flux of 4.9 m/s and 14.2 kg/m$^2$s. Simulations show that the granular temperature is high in the center, and low near the wall. Results simulated by the SOM model are larger than that by the KTGF.[39] The granular temperature was measured by means of a CCD from measured instantaneous particle velocities.[39] The instantaneous velocities of particles were computed from the measured streak lines traveled by the particles in a given time interval specified on the camera. The granular temperature is calculated from variances of velocity of particles. Measured granular temperature shows that the granular temperature is gradually increased toward the center, and then reduced in the center regime. The difference between the simulations and the measurements is obvious. Simulated results do not predict well the granular temperature in the annular region. The measured granular temperatures are smaller than that from simulations. Note that a high value of restitution coefficient is used in simulations. The energy dissipation during collisions relates with the restitution coefficient of particles. The restitution coefficient varies from zero to one: if it is equal to one, the collision is elastic, which means that there is no energy loss during collision, otherwise the collision is inelastic, which means that there is energy dissipation during collision. The energy dissipation is increased with the decrease of restitution coefficient. Therefore, the predictions overestimate the granular temperature.

There are three kinds of fluctuating energies in circulating fluidized beds[21]: (1) random oscillations (granular temperature) of individual particles, (2) turbulence caused by the motion of clusters, and (3) process induced fluctuations. The first two kinds of fluctuation of particles give rise to two kinds of motion of particles, motion on the level of particles and motion on the level of clusters. To account for the difference motions between particles and clusters in the riser, two different types of stresses of particles are used.[21] One is the particle stresses which are based on the calculation of the kinetic stresses. The shear and normal stresses of particles per unit bulk density are $C_iC_j = M_{ij}$ and $C_iC_i = M_{ii}$. Therefore, the normal components of the second-order moments give the particle normal stresses of particles. Such normal second-order moments are due to the oscillation of particles. The other is defined as the Reynolds stresses which are computed from the hydrodynamic velocities. The Reynolds stresses are calculated by averaging the hydrodynamic velocity for particles $u(r)$ from numerical simulations[21]

$$M_{b,ij} = \overline{u_i'u_j'}(x) = \frac{1}{T}\int_t^{t+T} u_i'u_j'(t,x)dt \tag{27a}$$

$$u_i'u_j'(t,x) = (u_i - \bar{u}_i)(u_j - \bar{u}_j) \tag{27b}$$

$$\bar{u}_i = \frac{1}{T}\int_t^{t+T} u_i(t,x)dt \tag{27c}$$

where $M_{b,ii}$ is the Reynolds stresses per unit bulk density. $u_i$ is the hydrodynamic velocity in $i$th-direction, $i$ or $j$ represents $x$ and $z$ directions (if $i = j$, $M_{b,ii}$ is the normal Reynolds stress; $i \neq j$, $M_{b,ij}$ is the shear Reynolds stress), and $T$ is the time interval. The predictions from the second-order moment method and experimental data[39] are plotted in Figure 11 at the superficial gas velocity and solid mass flux of 4.9 m/s and 14.2 kg/m$^2$s. From Figure 11 it can be seen that the predictions from the second-order moment method agree with the experimental data. The Reynolds stresses per unit bulk density $M_{b,zz}$ is on average a magnitude larger than the $M_{b,xx}$ in the $x$-direction. These Reynolds stresses represent the oscillations

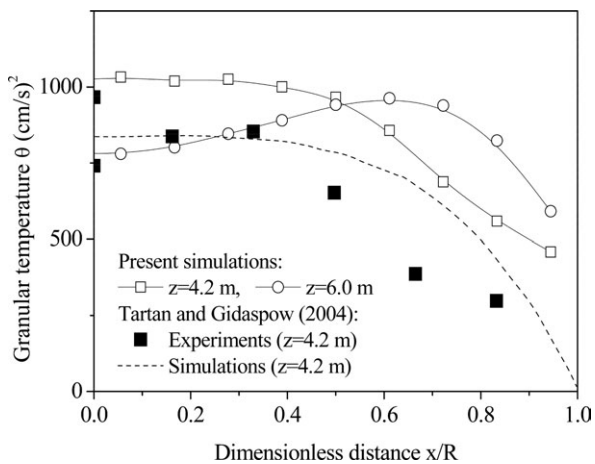


**Figure 10. Simulated and measured granular temperature of particles.**

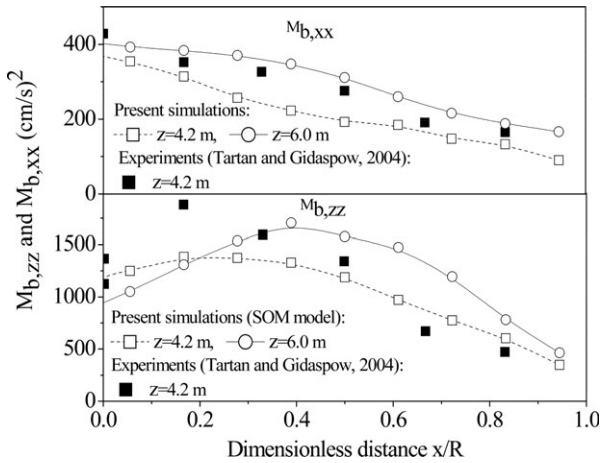


**Figure 11. Distribution of axial and radial normal Reynolds stresses.**

due to the macromotion of clusters. Thus, these high values of Reynolds stresses are due to the motion of clusters in the circulating fluidized bed. Comparing the normal second-order moments in Figure 8 to the normal Reynolds stress per unit bulk density in Figure 11, the normal Reynolds stress per unit bulk density has the same trends as the particle normal second-order moments. The large particle stresses per unit bulk density at the center show that mixing occurs due to particle oscillations in the riser.

The simulated shear Reynolds stress per unit bulk density, $M_{b,zx}$, and experimental data measured by Tartan and Gidaspow[39] is shown in Figure 12 at the gas velocity and solid mass flux of 4.9 m/s and 14.2 kg/m$^2$s. Both simulations and experiments show that the values $M_{b,zx}$ are low near the wall and the center, and high between them. Comparing to the particle normal second-order moments, the shear Reynolds stress per unit bulk density is low. The ratio of the normal Reynolds stresses in the axial direction to the normal Reynolds stresses in the radial direction is shown in Figure 12 at two different heights. The ratio $M_{b,zz}/M_{b,xx}$ is in the range of 2.5–7.5, and is in agreement with experiments.

The turbulent granular temperature is defined as the average of the normal Reynolds stresses

$$\theta_{t,}(x) = \frac{1}{3}\sum_{i=1}^{3} \overline{u_i' u_i'}(x) \tag{28a}$$

By assuming that the fluctuations are equal in the radial and the tangential directions, the definition can further be simplified to

$$\theta_{t,}(x) = \frac{1}{3}\overline{u_z' u_z'}(x) + \frac{2}{3}\overline{u_x' u_x'}(x) \tag{28b}$$

From computed Reynolds stress per unit bulk density, the turbulent granular temperature is calculated. Figure 13 shows the computed solid granular temperature $\theta$ and turbulent granular temperature $\theta_t$ as a function of concentration of particles at the gas velocity and solid mass flux of 4.9 m/s and 14.2 kg/m$^2$s. Roughly, the computed solid granular temperature increases, reaches a maximum, and then decreases with the increase of concentration of particles. Gidaspow and Huilin[22] showed that, in the dilute regions, the solid granular temperature is proportional to the concentration of particles raised to the power of 2/3 based on the KTGF. In the dense regions, the decrease in the granular temperature is due to the decrease of the mean free path of the particles. The trend of the computed results shown in Figure 11 agrees with the experimental results of Gidaspow and Huilin.[22] However, the computed turbulent granular temperature is roughly increased with the increase of concentration of particles. The principal characteristic of flow of particles is the production of additional stresses due to the velocity fluctuations caused by the formation of clusters. At the very low concentration of particles ($\varepsilon_s < 0.002$), the computed solid granular temperature is larger than the computed turbulent granular temperature. When the concentration of particles increases from a very dilute to a moderately dilute $\varepsilon_s < 0.0125$), the values of solid granular temperature are the same as the turbulent granular temperature. Further with the increase of concentration of particles, the solid granular temperature is decreased. However, the turbulent granular temperature increases with the increase of concentration of particles. The turbulent granular temperature is larger than the solid granular temperature. These two kinds of granular temperature give rise to

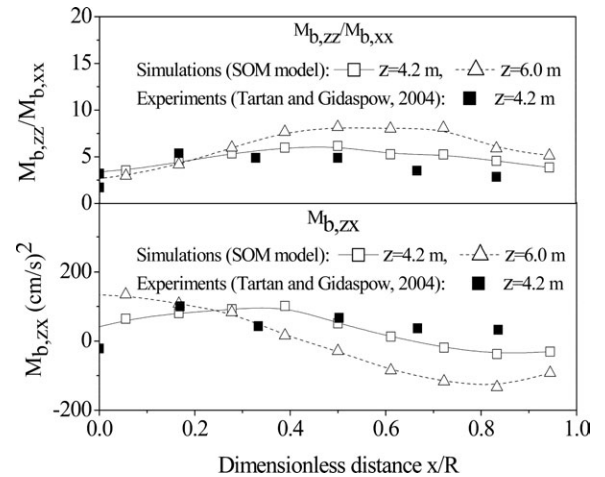


**Figure 12. Distribution of shear Reynolds stress and ratio of normal Reynolds stresses.**

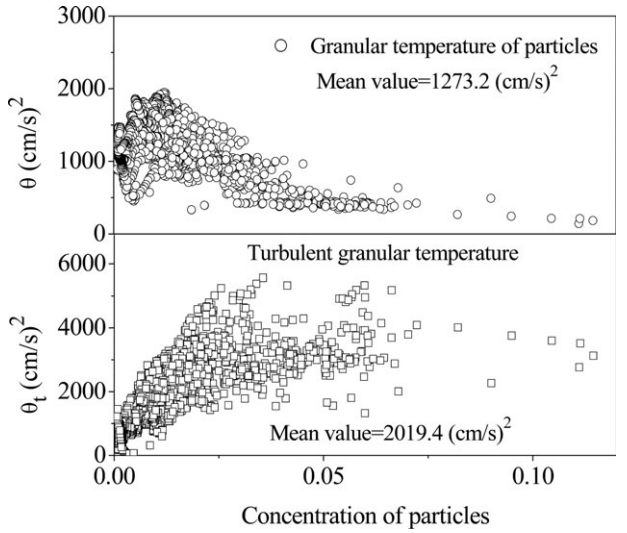


**Figure 13. Computed solid and turbulent granular temperatures.**

**Table 3. Simulation Parameters and System Properties in a Riser**

| Parameter | Experiments[40] | Present Simulations |
|---|---|---|
| Riser diameter | 15.2 cm | 15.2 cm |
| Riser height | 7.9 m | 7.9 m |
| Particle size | 150 $\mu$m | 150 $\mu$m |
| Particle density | 2550 kg/m$^3$ | 2550 kg/m$^3$ |
| Restitution coefficient | No | 0.95 |
| Normal restitution coefficient of wall-particles | No | 0.90 |
| Tangential restitution coefficient of wall-particles | No | 0.3 |
| Solid mass flux | 26.6 kg/m$^2$s | 26.6 kg/m$^2$s |
| Gas superficial velocity | 3.2 m/s | 3.2 m/s |
| Gas density | 1.2 kg/m$^3$ | 1.2 kg/m$^3$ |
| Stokes number $St$ | 3613 | 3613 |
| Reynolds number $Re_t$ | 23 | 23 |
| Time step | No | $1 \times 10^{-5}$ s |

two kinds of fluctuation, one on the level of particles and the other on the level of clusters. To compute the solid granular temperature, the second-order moment equations have to be programmed into the CFD codes. The code itself computes the classical solid granular temperature. At the high concentration of particles, the computed turbulent granular temperatures due to the cluster oscillations are higher than those due to particle oscillations. Most of the particles move as clusters in the riser. Hence, the turbulent granular temperature should dominate the oscillations in the riser. At the concentration from a very dilute to a moderately dilute, both granular temperatures are of the same order of magnitude. The oscillations by particles and clusters are about same throughout this riser. This is due to the fact that there is a coexistence of dilute (core) and dense (annular) phases in the riser. In the very dilute, the oscillations due to particles are high because of the available space between the particles.

### *Bhusarapu et al experiments in a circulating fluidized bed*

Solid flow dynamics are investigated in a cold circulating fluidized bed riser using noninvasive flow techniques.[40] The total height of the glass riser is 7.9 m and the internal diameter is 15.2 cm. Glass beads (Geldart B) with a mean diameter of 150 $\mu$m and particle density of 2550 kg/m$^3$ are used. Gamma ray computed tomography (CT) is used to measure the time-averaged cross-sectional solid concentration distribution. The time-averaged mean and fluctuating solid velocity fields have been quantified using the computer automated radioactive particle tracking (CARPT) technique. Detail descriptions of the experiments can be found in Bhusarapu et al.[40] The restitution coefficient of particles–particles and particles-wall are 0.95 and 0.9 which are used by Vaishali et al.[59] in simulations of riser. The parameters used in the present computations are given in Table 3.

Figure 14 shows the radial profile of concentration of particles at the superficial gas velocity and solid mass flux of 3.9 m/s and 33.7 kg/m$^2$s. Simulations show the distinctly higher concentration near the wall and also higher radial gradients. Experiments indicate that three distinct slopes in the profiles can be identified. Measured concentration of particle increases from the center, reaches a maximum and then decreases. When it reaches a minimum, and then increases toward the wall. The difference between the simulations using the SOM model and experiments is obvious. Simulations predicted by Vaishali et al.[59] are also given in by means of FLUENT 6.2 code. The difference between the predictions and experiments is clear. Present simulations using the SOM model over-predicate concentrations. Predictions by Vaishali et al.[59] are, however, under-predicted distribution of concentration in the riser.

Figure 15 shows a comparison between simulated time-averaged solid velocity and experiments at the superficial gas velocity and solid mass flux of 3.9 m/s and 33.7 kg/m$^2$s. The axial solid velocity component exhibits negative values near the wall. The axial solid velocity profiles seem roughly parabolic. It can be observed that the simulated solid axial components of the time-averaged axial velocity at the range of $x/R = 0.4$–$0.8$ are higher compared to experimental data. The predicted axial velocity of particles at the center and near the wall is close experiments. Simulations predicted by Vaishali et al.[59] are also given in using the commercial FLUENT 6.2 code. Both simulations and experiments show the axial velocity of particles is positive at the center and negative near the wall. The down-flow of solid at the wall is expected to cause a back-mixing of the solid phase. The discrepancy between the simulations predicted by Vaishali et al.[59] using KTGF and experiments from Bhusarapu et al.[40] is most likely because of the fact that the granular temperature models fluctuations in solid velocity under the assumption that the fluctuating kinetic energy has a Maxwellian distribution (inherent in the kinetic theory approaches). This assumption may no longer be valid for the current operating conditions.

From simulated instantaneous second-order moments, the time-averaged second-order moments are calculated. Figure 16 shows the radial profiles of the spatially averaged second-order moments at the superficial gas velocity and solid mass flux of 3.9 m/s and 33.7 kg/m$^2$ s. Simulations show that the normal second-order moment increases from the center, reaches a maximum, and then decreases near the wall. It can be clearly observed that the axial normal second-order moments are higher than the radial normal second-order moments. This is due to the high gradient in the axial solid velocity. While the radial velocities of particles are quite small and, hence their gradients are also small. Thus, the fluctuating motion is principally directed along the main axis of flow.

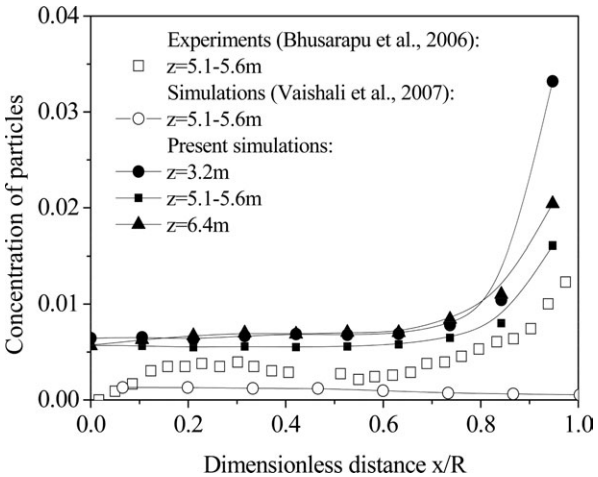


**Figure 14. Profile of simulated and measured concentration of particles.**

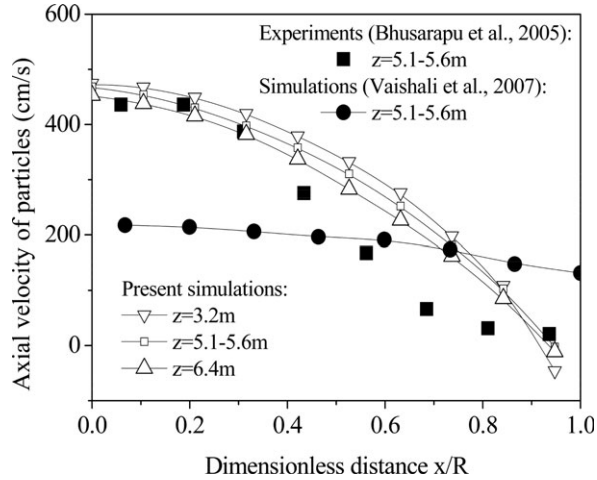


**Figure 15. Profile of simulated and measured time-averaged solid velocity.**

Figure 17 shows the simulated and measured ratio of normal second-order moments at the superficial gas velocity and solid mass flux of 3.9 m/s and 33.7 kg/m$^2$s. The averaged second-order moment, $\boldsymbol{M}_{\mathrm{av}} = \sum_{i=1}^{N} \boldsymbol{M}_i/N$, is calculated, where $N$ is the cell number along lateral direction. The difference between the simulations and the measurements is obvious in the center regime. The simulations are, however, close to measurements near the wall. Note that the simulated second-order moments are due to collisions of particles, while the measured values include not only the contributions of collisions of dispersed particles but cluster motions also. We see that at the dimensionless distance $x/R = 0.36$–$0.87$ the ratios of $M_{zz}/M_{zz,\mathrm{av}}$ and $M_{xx}/M_{xx,\mathrm{av}}$ are larger than 1.0. While near the wall and the center the ratios of $M_{zz}/M_{zz,\mathrm{av}}$ and $M_{xx}/M_{xx,\mathrm{av}}$ are smaller than 1.0. This indicates the second-order moments along axial and lateral directions are less than the sectional averaged second-order moments at the center and near the wall. Simulated results are in agreement with experiments except that the center regime of the riser.

Figure 18 shows profile of granular temperature at the superficial gas velocity and solid mass flux of 3.9 m/s and 33.7 kg/m$^2$s, respectively. The simulations from Vaishali et al.[59] are also shown in. A larger discrepancy is observed between

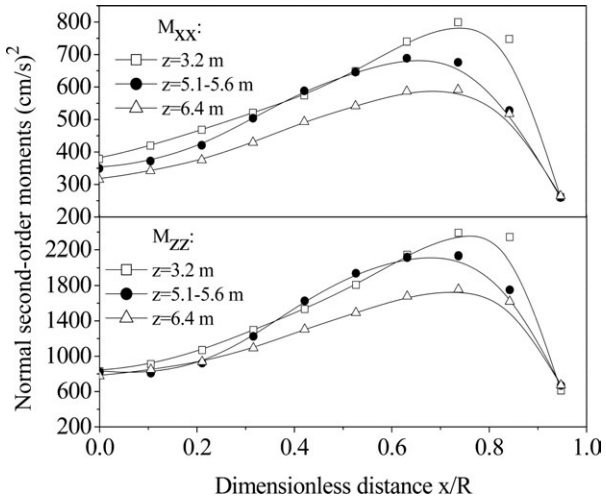


**Figure 16. Profiles of averaged normal second-order moments.**

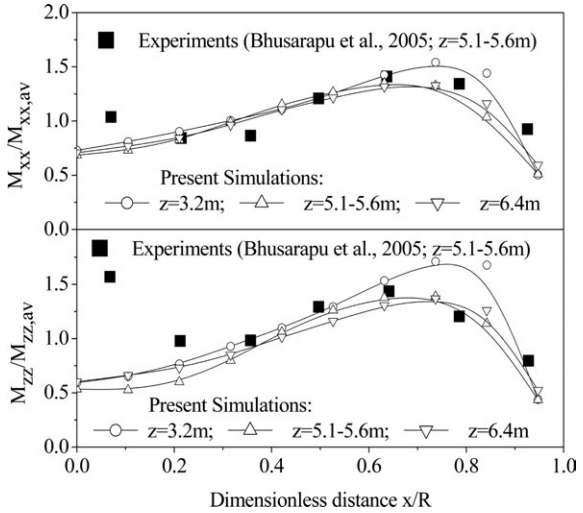


**Figure 17. Simulated and measured ratio of second-order moments.**

the SOM model and the KTGF by Vaishali et al.[59] Present simulations are in agreement with experimental data, although the predictions are over-predicted near the wall. Experiments and simulations show that the granular temperature increases from the center, reaches a maximum, and then decreases near the wall. This radial position, according to the radial profile of particle occurrence given in Figure 14, corresponds to the transition from a flat solid concentration profile to a drastically increasing one. Hence, the peak in the radial granular temperature profile corresponds to the transition from a lean core with nearly constant solid concentration to a dense zone with the increase of solid concentration. The granular temperature is over-predicted by Vaishali et al.[59] using KTGF. One possible reason for this over-prediction is the fact that the CARPT-measured granular temperature values are azimuthally averaged, whereas the CFD predicted granular temperature values are not. From Figure 16, it can be seen the axial second-order moments are always greater than the radial ones. The ratio of $M_{zz}/M_{xx}$ at $z = 3.2$ m is from 2.23 near the center to 3.1 near the annulus. The anisotropy is significant. This suggests that the second-order moment or "higher-order" moment CFD model is desired to predict the fluctuations of particles in risers.

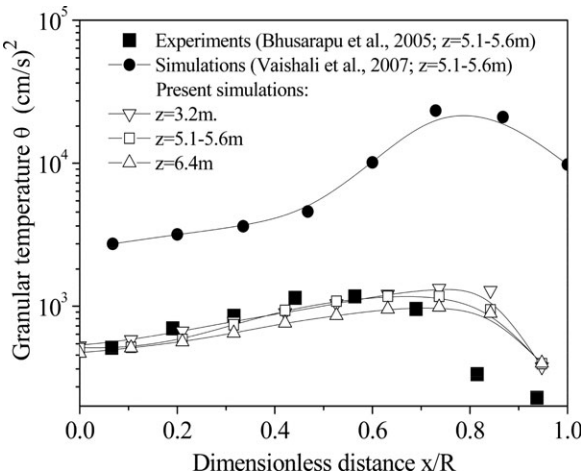


**Figure 18. Radial distribution of granular temperature.**

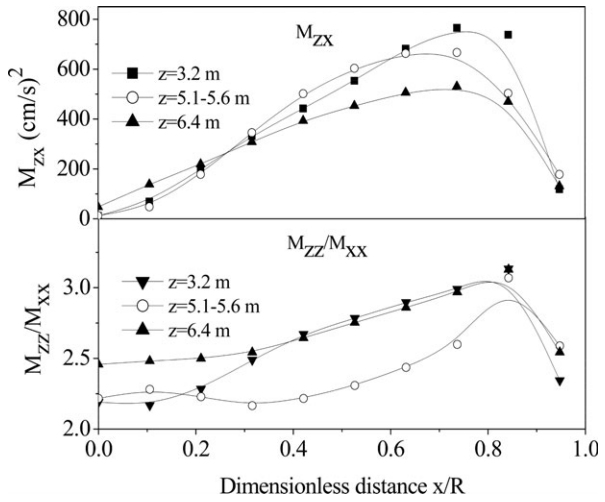


**Figure 19. Profile of ratio of second-order moments and second-order cross moments.**

Figure 19 shows the profile of ratio of axial and lateral second-order moments $M_{zz}/M_{xx}$ and second-order cross moments $M_{zx}$ at the superficial gas velocity and solid mass flux of 3.9 m/s and 33.7 kg/m$^2$s. The ratio of $M_{zz}/M_{xx}$ is in the range of 2.2–3.25. The axial component of second-order moments is higher than that lateral component. The second-order cross moment $M_{zx}$ is found to be higher at $x/R = 0.7$–0.82. The reason could be due to the solid concentration is rapidly increased, leading to significantly higher number of particle collisions. Hence, particle collisions are the controlling mechanism for momentum transfer due to the fluctuating velocities.

From the computed Reynolds stresses per unit bulk density $M_{b,ii}$, the turbulent granular temperature is calculated. Figure 20 shows the profile of solid granular temperature $\theta$ and turbulent granular temperature $\theta_t$ as a function of concentrations at the superficial gas velocity and solid mass flux of 3.9 m/s and 33.7 kg/m$^2$s. The mean turbulent granular temperature is 10 times of mean solid granular temperature in the riser. Roughly, both the solid granular temperature and the turbulent granular temperature increase at the low concentrations and decrease at the high concentration of particles. The observations from Figure 20 suggest that the peak in the granular temperature may occur around a value of solid concentration of 0.5–2.5% in the riser.

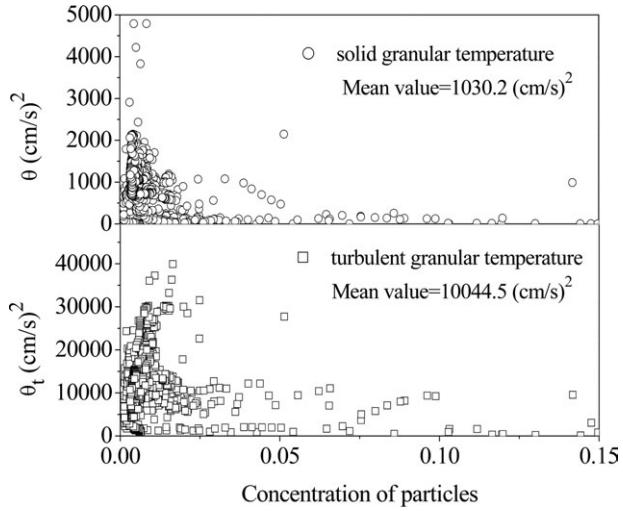


**Figure 20. Profile of granular temperature as a function of concentrations.**

**Table 4. Simulation Parameters and System Properties in a Vertical Pipe**

| Parameter | Experiments[41] | Present Simulations |
|---|---|---|
| Diameter of pipe | 30.5 mm | 30.5 mm |
| Height of pipe | 5.1 m | 5.1 m |
| Particle size | 500 $\mu$m | 500 $\mu$m |
| Particle density | 1020 kg/m$^3$ | 1020 kg/m$^3$ |
| Mass loading ratio | 1.1 and 2.0 | 1.1 and 2.0 |
| Gas velocity | 7.96 and 8.0 m/s | 7.96 and 8.0 m/s |
| Gas density | 1.2 kg/m$^3$ | 1.2 kg/m$^3$ |
| Restitution coefficient | No | 0.95 |
| Normal restitution coefficient of wall-particles | No | 0.90 |
| Tangential restitution coefficient of wall-particles | No | 0.1 |
| Stokes number $St$ | 23,010 | 23,010 |
| Reynolds number $Re_t$ | 334 | 334 |
| Time step | No | $1 \times 10^{-5}$ s |

### *Tsuji et al experiments in a vertical pipe*

Using a laser-Doppler velocimeter (LDV), Tsuji et al.[41] reported measurements of the flow properties in a fully developed, two-phase, air-particle turbulent flow in a 30.5 mm vertical pipe. In their experiments, the density and diameter of particles (Geldart B) were 1020 kg/m$^3$ and 500 $\mu$m, respectively. A restitution coefficient of $e = 0.95$ for particle–particle collisions and $e_{wn} = 0.9$ for particle-wall collisions are used in this simulation. The parameters used in the present computations are given in Table 4. Figure 21 shows the simulated and measured gas axial velocity at two mass loading ratios ($m = 1.1$ and 2.0) in a vertical pipe. Here, $u_c$ is the centerline gas velocity, and the Reynolds number based on mean gas velocity is $1.6 \times 10^4$. Simulations show the gas axial velocity is low near the wall, and increases toward the center of the pipe. Experiments give the gas velocity profile resembles that of a turbulent flow with a sharp gradient near the wall. The difference between simulations and experiments is obvious. The main reason is the effect of gas turbulence is not considered in simulations. For a gas–solid flow at the high gas velocity and low mass loading ratio, the gas turbulence is expected to have a noticeable effect on the momentum and energy transfer between both phases.[60] Therefore, for a flow at high Reynolds number, a suitable turbulence model for gas phase is needed.

The simulated and measured axial velocities of particles are also shown in Figure 21 at two mass loading ratios. Both simulations and experiments show the particle velocity profile decreases toward the wall. Compared to measured and simulated axial velocity of gas phase, in most parts of the pipe, the particle velocity is smaller than the air velocity. Comparing axial velocity of gas phase and particles, it is observed that the air velocity distribution becomes slightly more flat due to the presence of particles. The predicted axial velocity of particles is in agreement with experiments.

Figure 22 shows the profile of concentration of particles at two mass loading ratios across the pipe. It is observed that the concentration of particles is gradually increased toward the center of the pipe. The concentration of particles is increased with the increase of mass loading ratio. From simulations, the axial fluctuation velocity of particles is

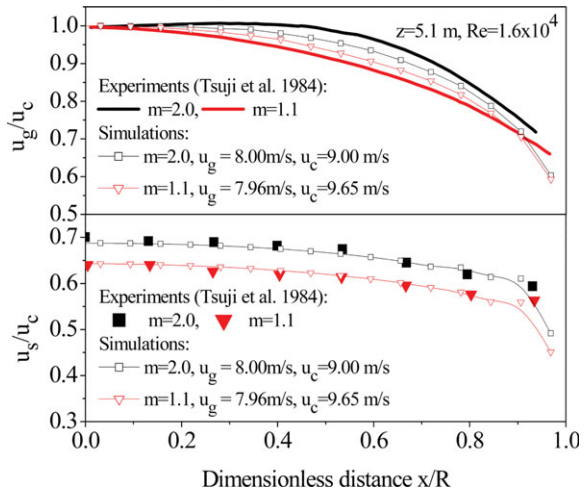


**Figure 21. Simulated and measured axial velocities of gas and particles.**

**[Color figure can be viewed in the online issue, which is available at wileyonlinelibrary.com.]**

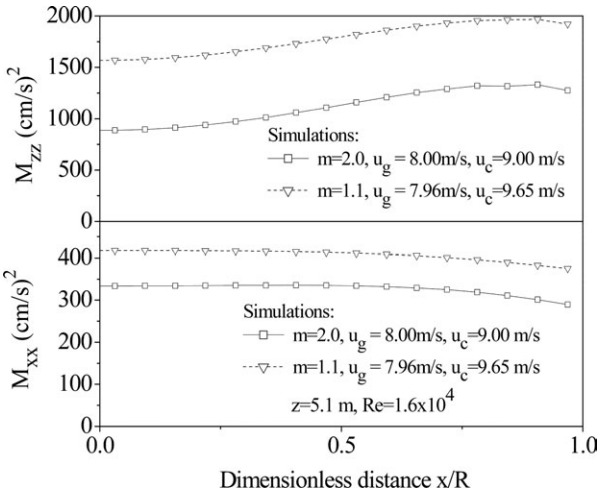


**Figure 23. Profile of normal second-order moments of particles.**

calculated. The calculated axial fluctuation velocity is also given in Figure 22 at two mass loading ratios. Roughly, the fluctuation velocity of particles decreases toward the center of the pipe. The fluctuation velocity of particles is decreased with the increase of mass loading ratio. This indicates in this case the presence of particles suppresses the fluctuation intensity of particles.

Figure 23 shows the simulated normal second-order moments of $M_{zz}$ and $M_{xx}$ at two mass loading ratios along lateral direction. It is observed that the second-order moment $M_{xx}$ is increased toward the center of the pipe, while the trend of the second-order moment $M_{zz}$ is reverse. Both $M_{xx}$ and $M_{zz}$ are decreased with the increase of mass loading ratio. The ratio of $M_{zz}/M_{xx}$ is calculated, and shown in Figure 24 at two mass loading ratios. The value of $M_{zz}/M_{xx}$ is decreased with the increase of mass loading ratio. The second-order cross moment $M_{zx}$ is also given in Figure 24 at two mass loading ratios. It is observed that the simulated second-order cross moment of particles is low at the wall,

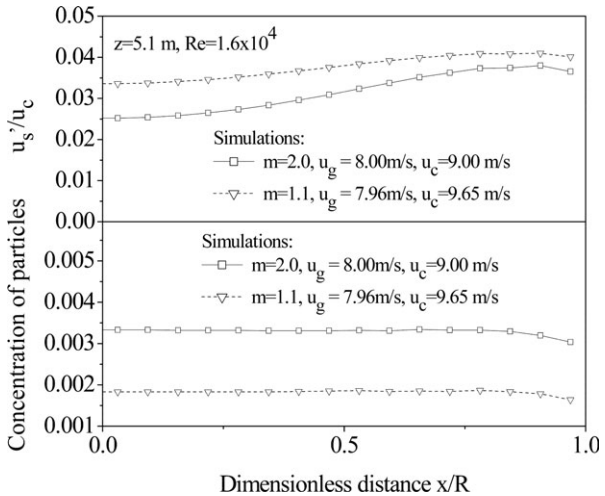


**Figure 22. Profile of concentration and axial fluctuation velocity of particles.**

and increases to its maximum value at about $x/R = 0.65$–$0.72$. It then decreases to zero at the centerline of the pipe. The decrease in $M_{zx}$ is observed when the mass loading ratio is increased. It is also noted that the value of $M_{zx}$ is smaller than the normal second-order moments $M_{xx}$ and $M_{zz}$. Thus, the above argument leads to the conclusion that although the mean velocity increases, the velocity fluctuations and second-order moments decrease with the increase in the solid mass loading.

### *Effect of closure correlations for third-order velocity moments*

From the kinetic theory of gases, the generic $(N+1)$th-order moment of the fluctuating velocities divided by $n$, besides the generic $(N+1)$th-order moment of the fluctuating velocities, is

$$\int C_k c_{i1} c_{i2} \cdots c_{iN} f^{(1)}(C, r, t) dC \tag{29}$$

From the elementary kinetic theory of gases, it is known that this value is equal to the diffusive flux along the $k$ direction of the property $C_{i1}C_{i2}\cdots C_{iN}$. We see that Eq. 29 gives the diffusive flux along the $k$ direction of the property $c_{i1}c_{i2}\cdots c_{iN}$. Based on concepts of the elementary kinetic theory proposed by Grad,[27] the diffusive flux along the $k$ direction is expressed by

$$\begin{aligned}&(\text{diffusive flux of the property } c_{i1}c_{i2}\cdots c_{iN} \text{ on the generic } k \text{ direction})\\ &= (\text{positive diffusive flux of particles on the k direction})\\ &\times (\text{difference of the mean value of the property } c_{i1}c_{i2}\cdots c_{iN})\end{aligned} \tag{30}$$

The distance on the generic $k$ direction between the mean position of the last collision of the particles that move in the "positive direction" with respect to $\mathbf{r}$ is $\ell_k^+$. while $\ell_k^-$ is the distance along $k$ in the "negative direction." Therefore, the difference of the mean value of the second-order moment $M_{ij}^{k^+} = (C_iC_j)^{k^+}$ has to be evaluated at $\ell_k^+$ (and, respectively, $M_{ij}^{k^-} = (C_iC_j)^{k^-}$ at $\ell_k^-$). Hence, neglecting external forces, the diffusive flux along the $k$ direction of the property $C_iC_j$ is

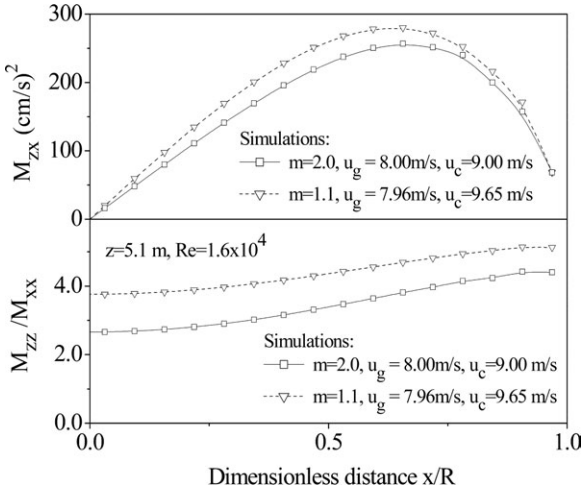


**Figure 24. Ratio of normal second-order moments and second-order cross moment of particles.**

$$M_{kij} = \frac{1}{n} \times (\text{diffusive flux of the property } C_iC_j \text{ on the } k \text{ direction})$$
$$= \frac{1}{n}\int_{C_k>0} C_k f d\mathbf{C} \times (C_iC_j)^{k^+} + \frac{1}{n}\int_{C_k<0} C_k f d\mathbf{C} \times (C_iC_j)^{k^-} \quad (31)$$

Here, we assume that the particle velocity probability density function equals to be the Maxwellian distribution function.

$$M_{kij} = \left(M_{ij}^{k^+} - M_{ij}^{k^-}\right)\frac{1}{n}\int_{C_k>0} C_k f d\mathbf{C}$$
$$= -\frac{\partial M_{ij}}{\partial x_k}(l_k^+ + l_k^-)\frac{1}{n}\int_{C_k>0} C_k f d\mathbf{C}$$
$$= -\left(l_k^+ + l_k^-\right)\sqrt{\frac{\theta}{8\pi}}\left(1 + \frac{M_{kk}}{\theta}\right)\frac{\partial M_{ij}}{\partial x_k} \quad (32)$$

The value of distance $\ell_k^+$ and $\ell_k^-$ can be estimated from the mean value of $(c_q t_c)$, where $c_q$ is the velocity at the point $\mathbf{r}$ of particles in time $dt$, and $t_c$ is the interval between the time of the last collision and the time in which the particle arrives at the point $\mathbf{r}$. This calculation can be approximated as the product of $<t_c>$ (the mean value of $t_c$ over the particles that travel in the positive direction) by $<c_q>$(the mean value of $c_q$ over all value of $c$). The first one, $<t_c>$, is estimated by $\tau_c$, the collision time (the mean time between two successive collisions) for particles. Thus, $\ell_k^+$ and $\ell_k^-$ are calculated as

$$l_k^{k+} = l_k^{k-} = K\tau_c \frac{1}{n}\int Cf d\mathbf{C} \quad (33)$$

where K is a constant. We assume that the particle velocity probability density function is the Maxwellian distribution function. Equation 33 can be evaluated analytically by means of known integrals.[30]

$$l_k^{k+} = l_k^{k-} = K\tau_c \frac{1}{n}\int Cf_0 d\mathbf{C} = K\tau_c\sqrt{\frac{8\theta}{\pi}} \quad (34)$$

where the constant K is 2.5 from the hard sphere collision theory.[1,2,37] Another parameter is the particle–particle collision time $\tau_c$. In the frame of the kinetic theory, the particle–particle collision time is

$$\tau_c = 1/\left[24\frac{\varepsilon_s g_0}{\sigma}\sqrt{\frac{\theta}{\pi}} - 4\varepsilon_s g_0 \nabla \cdot u_s\right] \quad (35)$$

From Eq. 32, it gives

$$M_{kij} = -\frac{5\sigma}{24\varepsilon_s g_0 - 4\varepsilon_s g_0 \sigma \nabla \cdot u_s\sqrt{\frac{\pi}{\theta}}}\sqrt{\frac{\theta}{\pi}}\left(1 + \frac{M_{kk}}{\theta}\right)\frac{\partial M_{ij}}{\partial x_k} \quad (36)$$

Comparing Eq. 36 with Eq. 18 and neglecting the velocity gradient effect, a factor, $1 + 6(1+e)\varepsilon,g_0/5$, is required. Therefore, from Eq. 36 the modified closure equation for the third-order velocity moment is expressed

$$M_{kij} = -\frac{\left[1 + \frac{6}{5}(1+e)\varepsilon_s g_0\right]}{\frac{2}{5\sigma}(1+e)\varepsilon_s g_0\sqrt{\pi\theta}(6 - \sigma\nabla \cdot u_s\sqrt{\frac{\pi}{\theta}})}(\theta + M_{kk})\frac{\partial M_{ij}}{\partial x_k} \quad (37)$$

which is known as model B.

Figure 25 shows the distribution of time-averaged concentration of particles of the riser at the superficial gas velocity and mass flux of 4.9 m/s and 14.2 kg/m$^2$s, respectively. Two different models of third-order velocity moment, model A and model B, are used. Qualitatively both models reveal the solid concentrations increase near the walls and are flat in the center region. The distributions seem to be nearly axisymmetric flow as predicted from the concentration distributions. Both the model A and model B give the same trends along lateral direction. Compared to the model B, the model A gives a high concentration of particles near the walls. The time-averaged axial velocity of particles is also shown in Figure 25. Simulations using the model A and model B give the same trends along lateral direction. The axial solid velocity exhibits negative values near the wall. Both models give

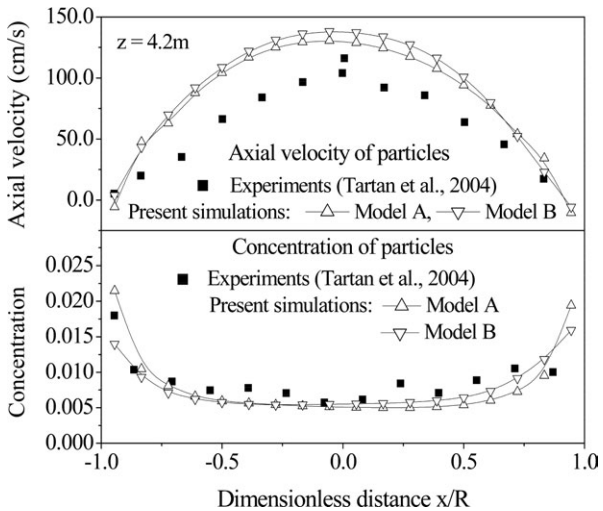


**Figure 25. Profile of concentration and axial velocity of particles.**

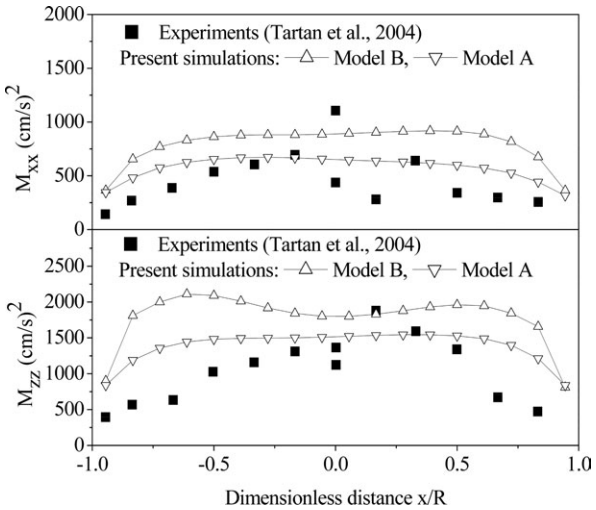


**Figure 26. Simulated and measured second-order moments in the riser.**

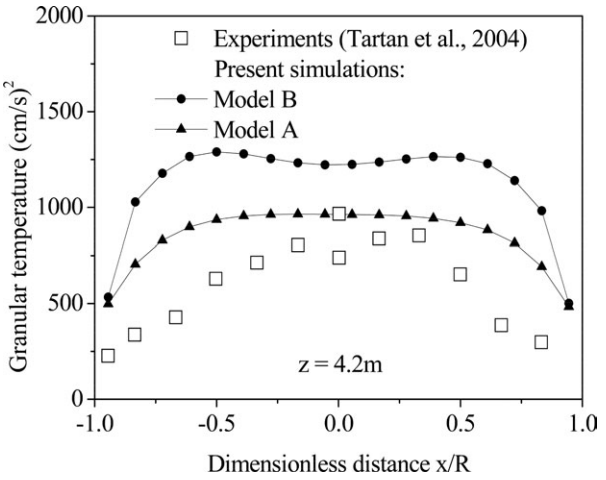


**Figure 27. Profile of granular temperature of particles.**

the axial solid velocity profiles seem roughly parabolic. The computed axial velocities of particles show a bell shape type profile with the upflow at the center and downflow near the wall. The axial velocity of particles predicted by the model A is lower near the center regime and larger near the walls than that from the model B. Hence, the down-flow of solid at the wall from the model A is expected to cause a high back-mixing of the solid phase in comparison with the model B. Both models confirm an axi-symmetric flow pattern of the solid in the riser.

Figure 26 compares the radial profiles of the averaged second-order moments from the model A and the model B at the superficial gas velocity and mass flux of 4.9 m/s and 14.2 kg/m$^2$s. Both models A and B show the radial second-order moments are large in the center regime and small near the walls. For the model A, simulations show that the axial normal second-order moments are large in the center and low near the walls. While the model B gives that the axial normal second-order moments increase, reach maximum, and then decrease toward the walls. The difference between two models is obvious. The model B gives a high second-order moments in comparison with the model A.

Figure 27 shows a comparison of the experimentally measured granular temperature θ to the simulations from the model A and the model B at the superficial gas velocity and mass flux of 4.9 m/s and 14.2 kg/m$^2$s. Computed results using the model A show that the granular temperature is low near the walls, and increases toward the center regime. While the model B gives that the granular temperature increases from the center, reaches maximum, and then decreases toward the walls. The difference between the simulations using the model A and the model B is obvious. The computed granular temperature using the model A is smaller than that by means of the model B. This means that the model B for the third-order moments over-estimates granular temperature in the riser.

In Eq. 37 for the model B, the term of the divergence of particle velocity $\nabla \cdot u_s$ in the denominator represents the influence of particle–particle collisional time. Figure 28 shows the profile of concentration and axial velocity of particles by means of the model B with and without the divergence of $u_s$ (Div $u_s$) term at the superficial gas velocity and solid mass flux of 4.5 m/s and 33.7 kg/m$^2$s. Both simulations give the concentration of particles is low in the center and high near the walls. The axial velocity of particles is positive in the center and negative near the walls. This indicates both simulations give particles up-flow in the center and down-flow near the walls. Comparing to simulations without Div $u_s$ term, the predicted concentration of particles with Div $u_s$ term is low in the center and large near the walls. The trend of predicted axial velocity of particles is reverse. However, we see that the difference between them is negligible. Therefore, the divergence of $u_s$ term in the model B is insignificant for simulations in risers.

From Eq. 20 for the model A, the first term in the denominator ($\beta$ term) represents the influence of particle inertia on the third-order moments of particles. This term with drag coefficient $\beta$ is important when particle motion is controlled by the aerodynamic forces. Figure 29 shows the distribution of concentration and second-order moment $M_{zz}$ predicted by the model A with and without $\beta$ term at the superficial gas velocity and solid mass flux of 4.5 m/s and 33.7 kg/m$^2$s. Simulations with and without $\beta$ term give a low concentration of particles in the center and large near the walls.

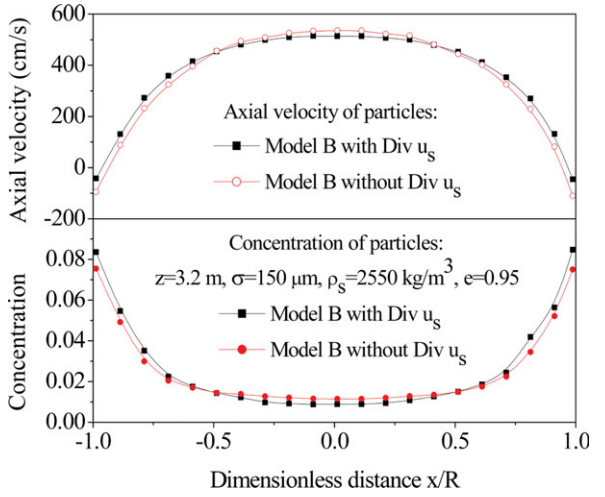


**Figure 28. Profile of concentration and axial velocity of particles using model B.**

**[Color figure can be viewed in the online issue, which is available at wileyonlinelibrary.com.]**

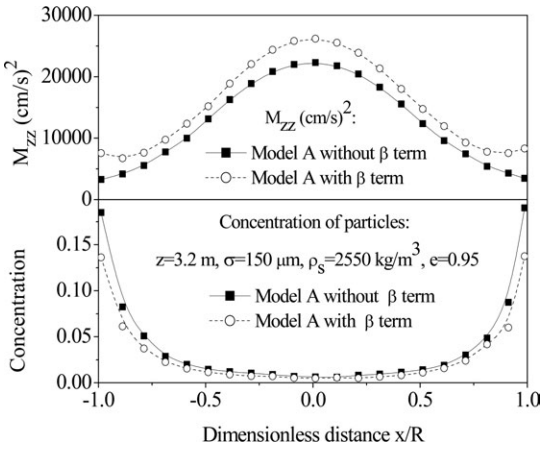


**Figure 29. Profile of concentration and second-order moment with and without $\beta$ term.**

Simulated concentration of particles by means of the model A is lower with $\beta$ term than that without $\beta$ term. The trends are, however, the same. Simulated normal second-order moment $M_{zz}$ is large in the center and low near the walls. The difference of $M_{zz}$ using the model A with and without $\beta$ term is obvious near the walls. Roughly, the second-order moments $M_{zz}$ predicted by the model A with $\beta$ term are larger than that without $\beta$ term. This means the model A with $\beta$ term gives a low concentration and high $M_{zz}$. The behavior of the concentration and normal second-order moment $M_{zz}$ is significantly affected.

It should be noted that in the model B, the third-order moments of particles can become infinite if denominator goes to zero (i.e., $\theta \rightarrow \pi\sigma^2(\nabla \cdot u_s)^2/36$). This causes the convergence problems in numerical simulations. There are a number of strategies to alleviate this problem. Here, we simply chose a limiter for the granular temperature between [$1.0 \times 10^{-6}$, $1.0 \times 10^{6}$] (m/s)$^2$ in the model B. This method did not seem to alter the accuracy of the simulated results. The choice of value of the limiter is the first we tried, and further validation might give slightly improved results.

### *Effect of interfacial work of gas–solid phases*

In Eq. (T1-5) for the second-order moments of particles, the fourth term represents the interaction with the continuous phase (a production or a destruction term). It splits into two terms. The first term represents the production due to the fluid-particle interactions, and the second term stands for the extra-dissipation due to the work done by the fluctuating drag force acting upon the particles in fluctuating motion. The expressions for the fluid-solid fluctuating velocity correlation, Eq. (T1-14), proposed by Koch and Sangani[43] are limited to small Reynolds numbers and large Stokes numbers, but they are algebraic. Therefore, for suspensions where these conditions are fulfilled, one does not need to solve a transport equation for the fluid-particle velocity correlation tensor.

Figure 30 shows the distribution of dimensionless second-order moments with and without the production due to the gas-particles interactions $\beta<C_gC_s>$ at the superficial gas velocity and solid mass flux of 4.9 m/s and 14.2 kg/m$^2$s. The axial component of second-order moments $M_{zz}$ is high in the center, and low near the walls. Both cases give the similar trends. With $\beta<C_gC_s>$, the dimensionless second-order moments $M_{zz}/\theta$ is larger than that without $\beta<C_gC_s>$. Assuming the particle response time tends to zero with respect to the eddy-particle interaction time, a closure model proposed by Simonin[60,61] is considered to simulate turbulent gas–solid flow in a vertical pipe.

$$\beta<C_{gi}C_{sj}>=\frac{\beta}{(\tau_x/\tau_{12})+(1+\varepsilon_s\rho_s/\varepsilon_g\rho_g)}\left(2k_f+3\frac{\varepsilon_s\rho_s}{\varepsilon_g\rho_g}\theta\right) \tag{38}$$

where $\tau_{12}$ is the time of interaction between particle motion and continuous phase fluctuations, and $\tau_x$ is the particle relaxation time.[49,62] Simulated results by means of Eq. 38 are also given in Figure 30. It can be seen that the dimensionless second-order moments $M_{zz}/\theta$ using Eq. 38 is lower than that with and without $\beta<C_gC_s>$. The second-order cross moment $M_{zx}$ is negative at $x/R < 0$, while it is reverse at $x/R > 0$. Near the walls, the second-order cross moment $M_{zx}$ is larger than that at the center regime of riser. The dimensionless second-order cross moment $M_{zx}/\theta$ is larger with $\beta<C_gC_s>$ than that without $\beta<C_gC_s>$. As it can be seen, the dimensionless second-order moments by means of the SOM with and without the production due to the gas-particles interactions $\beta<C_gC_s>$ and Eq. 38 are dependent of the model used to calculate the gas–solid velocity correlation. This term is very important for two-way coupling, and effect on the distribution of second-order moments of particles.

Indeed, the term $\beta<C_gC_s>$ appears in the interfacial terms of the transport equations for the fluctuating motion and can give production or destruction of the velocity fluctuations in both phases. More detailed models for the fluid-solid velocity correlation can be proposed by developing the transport equations for $<C_gC_s>$.[49,60–62] This fluid-particle velocity correlation tensor depends upon the production caused by the mean velocity gradients of the solid and the gas phases, the interaction between the second-order velocity moment in the solid phase, the production/destruction caused by the interaction of the solid phase with the gas phase, and the effects of the fluctuating pressure gradient, viscosity and crossing trajectories. The formulations proposed by Koch and Sangani[48] are given for dilute flows, where the influence of particle–particle collisions can be neglected. As the suspension becomes denser, the effect of collisions should influence the fluid-particle velocity correlation tensor. When solving the transport equations for the second-order velocity

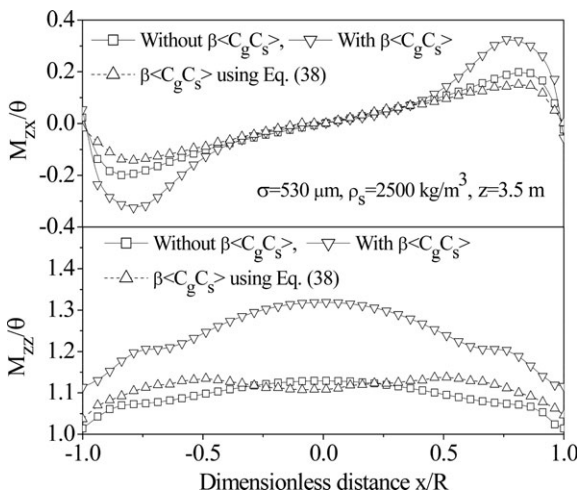


**Figure 30. Profile of second-order moments of particles.**

moment, the fluid-particle velocity correlation tensor appears in the coupling term. Thus, more research is needed to analyze the effect of the gas-particle interactions on hydrodynamics of gas and solid phases in the risers.

## Conclusions

A second-order moment method is proposed for computing flow of particles in the risers. With the KTGF, transport equations for the velocity moments and closure equations are derived for the particle phase. A third-order moment model is proposed with the consideration of the increase of the binary collision probability through the correlation of particle velocity. For the gas-particle velocity correlation, an algebraic model proposed by Koch and Sangani[48] is used. The boundary conditions for the set of equations describing flow of particles proposed by Strumendo and Canu[30] are modified with the consideration of the collisional energy exchange between the wall and the particles. The model for second-order moments is almost free from empirical constants, only the restitution coefficient has to be given. Present second-order moment model can be recovered to the original kinetic theory of slightly inelastic, perfectly smooth spheres for the isotropic flow of particles.

A two-dimensional (2-D) computational fluid dynamics (CFD) model with the second-order moment model of particles is used to simulate flow behavior of gas and particles in the riser. The distributions of concentration, velocity and moments of particles are predicted. Simulations indicate that the anisotropy is obvious in the risers. The Reynolds normal stresses per unit bulk density are computed from the simulated hydrodynamic velocities. For 530 $\mu$m particles in a riser measured by Tartan and Gidaspow,[39] the simulated second-order moment in the vertical direction is 1.1–2.5 times larger than that in the lateral direction, and the Reynolds normal stresses per unit bulk density are 2.2–8.5 times larger than that in the lateral direction in a riser. The ratio of the second-order moments along axial and lateral directions to the mean second-order moments is in the range of 0.5–1.5 for 150 $\mu$m particles in a riser measured by Bhusarapu et al.[40] The Reynolds normal stresses per unit bulk density have much higher values than that predicted by the second-order moment method. The predictions are in agreement with experimental normal second-order moments measured by Tartan and Gidaspow[39] and granular temperature of particles measured by Bhusarapu et al.[40] in risers. The SOM model is validated by comparing its predictions to experiments measured by Tsuji et al.[41] in a vertical pipe. Simulations show that an increase in the solid-phase concentration dampens the gas-phase velocity fluctuations far from the pipe wall. Simulated velocity is in accordance with experimental observations.

In principle, the second-order moments model can be used to solve flow problem, that is, modeled by a two-fluid approach. However, the limitations of present second-order moments mostly result from the assumptions made to derive this theory: flows with small spatial gradients, nearly elastic particles, binary collisions and a simplified model of particle–particle collision. A more general formulation could be achieved by a more advanced particle velocity distribution, but mathematical difficulties are encountered. More research is needed to derive a general model of the particle–particle interactions. The gas turbulence is concerned in the numerical simulations. In this case, separate equations for the turbulent stresses have to be solved. A three-dimensional (3-D) simulation might be useful to study the role of cluster structures and their role on flow behavior in risers. Nevertheless, more simulations and experimental measurements are required to improve the applicability of moment closures in further works.

In this regard, we would like to cite the recent work of Fox and coworkers, who have in part addressed gas–solid flows using quadrature method of moments.[34–36] They have successfully solved dilute to moderately dilute gas-particle flow. In these studies, they did not use Grad's theory to deal with the velocity moments, because their systems of interest were dilute or moderately dilute, and, therefore, the Knudsen number was not sufficiently small for these methods to hold; they adopted, conversely, quadrature formulas to approximate the velocity distributions. These analyzes are important for using Eulerian multifluid models to treat dilute systems leads to incorrect results caused by the inability of these models to capture particle trajectory crossing. Desjardins et al.[35] showed that the assumption that a gas-particle flow can be described accounting for only the mean momentum of the particle phase leads to incorrect predictions of all the velocity moments, including the particle number density, showing the need of using a multivelocity method, to correctly capture the physics of the flow. Similar observations were made for moderately collisional gas-particle flows by Sakiz and Simonin.[33] However, for a flow of gas and particles in risers, such as those considered in this work, the method of Grad is used since it gives direct access to the moments. The major drawbacks of the method of moments used are due to the simple collision model (no friction) and low level of anisotropy. We believe that more research is needed to render the KTGF more general for an improvement of the Eulerian–Eulerian formulation.

## Acknowledgments

This work was supported by Natural Science Foundation of China through Grant no.51076040 and 51176042.

## Notation

$a_{ij}$ = second-order coefficient, $m^2/s^2$
$a_{ijm}$ = third-order coefficient, $m^3/s^3$
$c$ = velocity of particle, m/s
$C$ = fluctuation velocity of particle, m/s
$e$ = particle–particle restitution coefficient
$e_w$ = wall-particle restitution coefficient
$f$ = single particle distribution function, $s^3/m^6$
$f^{(2)}$ = pair distribution function, $s^6/m^{12}$
$F$ = external force acting on a particle per mass unit, N/kg
$g$ = gravitational acceleration, $m/s^2$
$g_0$ = radial distribution function
$H^{(N)}$ = Hermite polynomial of order N
$k$ = particle collision unit vector
$k_f$ = gas-phase turbulent kinetic energy, $m^2/s^2$
$Ma$ = Mach number
$M_{b,ij}$ = Reynolds stresses, $m^2/s^2$
$M_{ij}$ = second-order moment, $m^2/s^2$
$m$ = mass loading ratio
$m_s$ = mass of a particle, kg
$n$ = number of particles per unit volume, $1/m^3$
$N$ = number
$p_g$ = gas pressure, Pa
$R$ = radii (m)
$Re$ = Reynolds number
$St$ = Stokes number
$t$ = time, s
$u_g$ = gas velocity and superficial gas velocity, m/s
$u_s$ = particle velocity, m/s

$u_t$ = terminal velocity of an isolated particle, m/s
$x,y,z$ = spatial coordinate, m

### Greek letters

$\theta$ = granular temperature, $m^2/s^2$
$\theta_t$ = turbulent granular temperature, $m^2/s^2$
$\sigma$ = particle diameter, m
$\varepsilon_s$ = concentration of particles
$\varepsilon_g$ = porosity
$\delta_{ij}$ = Kronecker's symbol
$\mu_g$ = kinematic viscosity of gas phase, Pa s
$\rho$ = density, $kg/m^3$
$\phi$ = transported property
$\tau$ = stress tensor, $N/m^2$
$\beta$ = drag coefficient, $kg/m^3s$
$\varphi$ = switch function

### Subscripts

g = gas phase
$n$ = normal direction
s = particles phase
t = tangential direction
w = Wall

## Literature Cited


1. Gidaspow D. *Multiphase Flow and Fluidization: Continuum and Kinetic Theory Descriptions*. Academic Press: San Diego, 1994.
2. Chapman S, Cowling TG. *The Mathematical Theory of Non-Uniform Gases*. Cambridge University Press: Cambridge, UK, 1970.
3. Sinclair JL, Jackson R. Gas-particle flow in a vertical pipe with particle-particle interactions. *AIChE J*. 1989;35:1473–1486.
4. Ding J, Gidaspow D. Bubbling fluidization model using kinetic theory of granular flow. *AIChE J*. 1990;36:523–538.
5. Mathiesen V, Solberg T, Arastoopour H, Hjertager BH. Experimental and computational study of multiphase gas/particle flow in a CFB riser. *AIChE J*. 1999;45:2503–2518.
6. Benyahia S, Arastoopour H, Knowlton TM, Massah H. Simulation of particles and gas flow behavior in the riser section of a circulating fluidized bed using the kinetic theory approach for the particulate phase. *Powder Technol*. 2000;112:24–33.
7. Van Wachem GGM, Schoute JC, Van den Bleek CM, Krishna R, Sinclair JL. Comparative analysis of CFD models of dense gas-solid systems. *AIChE J*. 2001;47:1035–1051.
8. Agrawal K, Loezos PN, Syamlal M, Sundaresan S. The role of meso-scale structures in rapid gas-solid flows. *J. Fluid Mech.* 2001;445:151–181.
9. Andrews AT, Loezos PN, Sundaresan S. Coarse-grid simulation of gas-particle flows in vertical risers. *Ind Eng Chem Res*. 2005;44:6022–6037.
10. Goldschmidt MJV, Kuipers JAM, Van Swaaij WPM. Hydrodynamic modeling of dense gas-fluidized beds using the kinetic theory of granular flow: effect of coefficient of restitution on bed dynamics. *Chem Eng Sci*. 2001;56:571–578.
11. De Wilde J, Marin GB, Heynderickx GJ. The effects of abrupt T-outlets in a riser: 3D simulation using the kinetic theory of granular flow. *Chem Eng Sci*. 2003;58:877–885.
12. Huilin L, Gidaspow D, Bouillard J, Wentie L. Hydrodynamic simulation of gas-solid flow in a riser using kinetic theory of granular flow. *Chem. Eng. J*. 2003;95:1–13.
13. Sun J, Battaglia F. Hydrodynamic modeling of particle rotation for segregation in bubbling gas-fluidized beds. *Chem Eng Sci*. 2006;61:1470–1479.
14. Lindborg H, Lysberg M, Jakobsen HA. Practical validation of the two-fluid model applied to dense gas-solid flows in fluidized beds. *Chem Eng Sci*. 2007;62:5854–5869.
15. Leboreiro J, Joseph GG, Hrenya CM. Revisiting the standard drag law for bubbling, gas-fluidized beds. *Powder Technol*. 2008;183:385–400.
16. Reuge N, Cadoret L, Coufort-Saudejaud C, Pannala S, Syamlal M, Caussat B. Multifluid Eulerian modeling of dense gas-solids fluidized bed hydrodynamics: Influence of the dissipation parameters. *Chem Eng Sci*. 2008;63:5540–5551.
17. Hartge EU, Ratschow L, Wischnewski R, Werther J. CFD-simulation of a circulating fluidized bed riser. *Particuology*. 2009;7:283–296.
18. Passalacqua A, Fox RO, Garg R, Subramaniam S. A fully coupled quadrature-based moment method for dilute to moderately dilute fluid-particle flows. *Chem Eng Sci*. 2010;65:2267–2283.
19. Vun S, Naser J, Witt P. Extension of the kinetic theory of granular flow to include dense quasi-static stresses. *Powder Technol*. 2010;204:11–20.
20. Arastoopour H. Numerical simulation and experimental analysis of gas/solid flow systems: 1999 fluor-Daniel plenary lecture. *Powder Technol*. 2001;119:59–67.
21. Gidaspow D, Jung J, Singh RK. Hydrodynamics of fluidization using kinetic theory: an emerging paradigm 2002 Flour-Daniel lecture. *Powder Technol*. 2004;148:123–141.
22. Gidaspow D, Huilin L. Collisional viscosity of FCC particles in a CFB. *AIChE J*. 1996;42:2503–2513.
23. Jung J, Gidaspow D, Gamwo IK. Measurement of two kinds of granular temperatures, stresses, and dispersion in bubbling beds. *Ind Eng Chem Res*. 2005;44:1329–1341.
24. Xie L, Biggs MJ, Glass D, McLeod AS, Egelhaaf SU, Petekidis G. Granular temperature distribution in a gas fluidized bed of hollow microparticles prior to onset of bubbling. *Europhys. Lett*. 2006;74:268–274.
25. Holland DJ, Muller CR, Dennis JS, Gladden LF, Sederman AJ. Spatially resolved measurement of anisotropic granular temperature in gas-fluidized beds. *Powder Technol*. 2008;182:171–181.
26. Grad H. On the kinetic theory of rarefied gases. *Commun Pure Appl Math*. 1949;2:331–407.
27. Jenkins JT, Richman MW. Grad's 13-moment system for a dense gas of inelastic spheres. *Archive Ration Mech Anal*. 1985;87:355–377.
28. Jenkins JT, Richman MW. Plane simple shear of smooth inelastic circular disks: the anisotropy of the second moment in the dilute and dense limits. *J Fluid Mech*. 1988;192:313–328.
29. Richman MW. Source of second moment in dilute granular flows of highly inelastic spheres. *J Rheol*. 1989;33:1293–1306.
30. Strumendo M, Canu P. Method of moments for the dilute granular flow of inelastic spheres. *Phys Rev E*. 2002;66:041304/1–041304/20.
31. Strumendo M, Gidaspow D, Canu P. Method of moments for gas-solid flows: application to the riser. Presented at the International Fluidization XI Conference, Ischia, Italy, May 9–14, 2004.
32. Simonin O. Prediction of the dispersed phase turbulence in particle-laden jets. In: *Proceedings of the 4th International Symposium on Gas-Solid Flows, ASME-FED*, Vol. 121, 1991:197–206.
33. Sakiz M, Simonin O.Numerical experiments and modeling of nonequilibrium effect in dilute granular flows. Presented at the 21st International Symposium on Rarefied Gas Dynamics, Toulouse, France, July 26–31, 1998.
34. Fox RO. A quadrature-based third-order moment method for dilute gas-particle flows. *J Comput Phys*. 2008;227:6313–6350.
35. Desjardin O, Fox RO, Villedieu P. A quadrature-based moment method for dilute fluid-particle flows. *J Comput Phys*. 2008;227:2524–2539.
36. Fox RO, Vedula P. Quadrature-based moment model for moderately dense polydisperse gas-particle flows. *Ind Eng Chem Res*. 2010;49:5174–5187.
37. Dan S, Shuyan W, Huilin L, Zhiheng S, Xiang L, Shuai W, Yunhua Z, Lixin W. A second-order moment method of dense gas-solid flow for bubbling fluidization. *Chem Eng Sci*. 2009;64:5013–5027.
38. Dan S, Jianzhi W, Huilin L, Yunhua Z, Juhui C, Gidaspow D, Ming C. Numerical simulation of gas-particle flow with a second-order moment method in bubbling fluidized beds. *Powder Technol*. 2010;199:213–225.
39. Tartan M, Gidaspow D. Measurement of granular temperature and stresses in risers. *AIChE J*. 2004;50:1760–1775.
40. Bhusarapu S, Al-Dahhan MH, Dudukovic MP. Solids flow mapping in a gas-solid riser: mean holdup and velocity fields. *Powder Technol*. 2006;163:98–123.
41. Tsuji Y, Morikawa Y, Shiomi H. LDV measurements of an air-solid two phase flow in a vertical pipe. *J Fluid Mech*. 1984;139:417–434.
42. Drew D. Mathematical modeling of two-phase flow. *Annu Rev Fluid Mech*. 1983;15:261–291.
43. Ergun S. Fluid flow through packed columns. *Chem Eng Proc*. 1952;48:89–94.
44. Wen CY, Yu YH. Mechanics of fluidization. *AIChE Ser*. 1966;62:100–111.
45. Huilin L, Yurong H, Gidaspow D. Hydrodynamic modelling of binary mixture in a gas bubbling fluidized bed using the kinetic theory of granular flow. *Chem Eng Sci*. 2003;58:1197–1205.

46. Heynderickx GJ, Das AK, De Wilde J, Marin GB. Effect of clustering on gas-solid drag in dilute two-phase flow. *Ind Eng Chem Res*. 2004;43:4635–4646.
47. Sangani AS, Mo G, Tsao HK, Koch DL. Simple shear flows of dense gas-solid suspensions at finite Stokes numbers. *J Fluid Mech*. 1996;313:309–341.
48. Koch DL, Sangani AS. Particle pressure and marginal stability limits for a homogeneous monodisperse gas-fluidized bed: kinetic theory and numerical simulations. *J Fluid Mech*. 1999;400:229–263.
49. Peirano E, Leckner B. Fundamentals of turbulent gas-solid flows applied to circulating fluidized bed combustion. *Prog. Energy Comb Sci*. 1998;24:259–296.
50. Strumendo M.Method of moments for gas-solid flows, PhD Dissertation, University of Padua, 2004.
51. Harlow FH, Amsden AA. Numerical calculation of multiphase fluid flow. *J Comput Phys*. 1975;17:19–52.
52. Harlow FH, Amsden AA. A numerical fluid dynamics calculation method for all flow speeds. *J Comput Phys*. 1971;8:197–213.
53. Sakiz, M., Simonin, O. Continuum modeling and Lagrangian simulation of massive frictional colliding particles in a vertical gas-solid channel flow, *Proc. 4th Int. Conf. on Multiphase Flow, New Orleans*. May 27- June 1, 2001.
54. Sakiz M, Simonin O.Continuum modeling and Lagrangian simulation of massive frictional colliding particles in a vertical gas-solid channel flow. In: *Proceedings of the 4th International Conference on Multiphase Flow, New Orleans,* 2001.
55. Lostec NL, Villedieu P, Simonin O.Comparison between Grad's and quadrature-based methods of moments for the numerical simulation of unsteady particle-laden flows. In: *Proceedings of the ASME 2009 Fluids Engineering Division Summer Meeting*, August 2–6, Vail, CO, 2009.
56. Patankar SV. *Numerical Heat Transfer and Fluid Flow*. Washington: Hemisphete, 1980.
57. Goldschmidt MJV, Beetstra R, Kuipers JAM. Hydrodynamic modeling of dense gas-fluidized beds: comparison and validation of 3D discrete particle and continuum models. *Powder Technol*. 2004;142:23–47.
58. Breault RW, Ludlow CJ, Yue PC. Cluster particle number and granular temperature for cork particles at the wall in the riser of a CFB. *Powder Technol*. 2005;149:68–77.
59. Vaishali S, Roy S, Bhusarapu S, Al-Dahhan MH, Dudukovic MP. Numerical simulation of gas-solid dynamics in a circulating fluidized-bed riser with Geldart group B particles. *Ind Eng Chem Res*. 2007;46:8620–8628.
60. Simonin O.Continuum modelling of dispersed turbulent two-phase flows, Technical Report, Lecture Series 1996–02, Laboratoire National d'Hydraulique–EDF 6 Quai Watier-78400 Chatou/France, 1996.
61. Simonin O, Deutsch E, Minier JR. Eulerian prediction of the fluid/particle correlated motion in turbulent two-phase flows. *Appl Sci Res*. 1993;51:275–283.
62. Benavides A, van Wachem B. Numerical simulation and validation of dilute turbulent gas-particle flow with inelastic collisions and turbulence modulation. *Powder Technol*. 2008;182:294–306.

*Manuscript received Apr. 5, 2011, and revision received Nov. 28, 2011, and final revision received Jan. 20, 2012.*